November 2015

Sedimentological Records and Numerical Simulations of the C.E. 1707 Hōei Tsunami in Southwestern Japan

Hannah Baranes
University of Massachusetts Amherst

SEDIMENTOLOGICAL RECORDS AND NUMERICAL SIMULATIONS OF THE C.E. 1707 HŌEI TSUNAMI IN SOUTHWESTERN JAPAN

A Thesis Presented

By

HANNAH ELIZABETH BARANES

Submitted to the Graduate School of the
University of Massachusetts Amherst in partial fulfillment
of the requirements for the degree of

MASTER OF SCIENCE

September 2015

Department of Geosciences

SEDIMENTOLOGICAL RECORDS AND NUMERICAL SIMULATIONS OF THE C.E. 1707 HŌEI TSUNAMI IN SOUTHWESTERN JAPAN

A Thesis Presented

By

HANNAH ELIZABETH BARANES

Approved as to style and content by:

_____

Jonathan D. Woodruff, Chair

_____

William D. McCoy, Member

_____

William P. Clement, Member

_____

Julie Brigham-Grette, Department Head, Geosciences

ACKNOWLEDGEMENTS

This research was made possible by the dedication and enthusiasm of many individuals, whom I feel grateful to have worked alongside. First, I would like to extend a heartfelt thank you to my advisor Dr. Jonathan Woodruff. Jon, you are a brilliant scientist, teacher, and mentor, and I cannot thank you enough for all you have taught me. I would also like to thank the many faculty members from UMass and beyond who contributed to and provided guidance for this work. Thank you to my committee members, Drs. William McCoy and William Clement, and thank you to Dr. Kinuyo Kanamaru, who spent countless hours organizing coring expeditions to southwestern Japan, translating Japanese documents, and discussing results. Along with Drs. Woodruff and Kanamaru, Dr. Timothy Cook from Worcester State University and Dr. Davin Wallace from the University of Southern Mississippi collected and performed initial analyses on many of the sediment cores used in this study, and they subsequently provided thoughtful comments on Chapter 1 of this manuscript.

I would also like to thank Dr. Jack Loveless from Smith College, Dr. Robert Weiss and Wei Cheng from Virginia Tech, and Dr. Bill Clement from UMass for helping me run numerical tsunami simulations. In one short month and through 64 emails, Jack taught me the basics of earthquake modeling and provided me with all of the calculations for initiating tsunami simulations from the earthquake scenarios presented in Chapter 2. Robert and Wei provided me with valuable guidance and computing power for running tsunami simulations in GeoClaw, and Bill helped me work through quite a few coding snafus as I was getting GeoClaw up and running.

Thank you to Ms. Kimura, Mr. Miyazaki, Dr. Akiko Okusu, Masako Okusu, Megumi Okamoto, and Sayaka Shimamoto for their assistance in the field, and thank you to Nina Schulze, Tommy Witten, Ashlyn Stromgren, Shohini Kundu, Hayli Kinney, Shuji Seto, and the UMass undergraduate sedimentology honors students for their help with laboratory and data analyses – their brightness and enthusiasm kept me excited to come into work each day of the last two years. Finally, thank you to Dr. Takahashi and to the residents and town officials of Yahatahama City and Ikata Town for their support of this research. Funding was primarily provided by the Risk Prediction Initiative, with additional funds from the Massachusetts Space Grant Consortium and the Japan Nuclear Regulations Authority.

ABSTRACT

SEDIMENTOLOGICAL RECORDS AND NUMERICAL SIMULATIONS OF THE C.E. 1707 HŌEI TSUNAMI IN SOUTHWESTERN JAPAN

SEPTEMBER 2015

HANNAH ELIZABETH BARANES, B.A. DARTMOUTH COLLEGE

M.S., UNIVERSITY OF MASSACHUSETTS AMHERST

Directed by: Assistant Professor Jonathan D. Woodruff

A tsunami generated by the C.E. 1707 Hōei earthquake is largely thought to be the flood event of record for southwestern Japan, yet historical documentation of the event is scarce. This is particularly true in northwestern Shikoku within the Bungo Channel, where significant inconsistencies exist between historical records and model-derived tsunami heights. Here, we present the first independent, geologic evidence of the Hōei tsunami in the Bungo Channel using complementary reconstructions of coastal inundation from three back-barrier lakes: Lake Ryuuoo, Lake Amida, and Lake Kamega. At all three sites, the most prominent marine overwash deposit of the past ~1,000 years, as defined by grain size, density, and geochemical indicators, is consistent with the timing of the C.E. 1707 event and provides strong evidence that the 1707 tsunami caused the most significant flooding of the last millennium in this region. At Lake Ryuuoo, modern barrier beach elevations and grain sizes in the tsunami's resultant deposit also provide ~4 m as the first physically based height constraint for the 1707 tsunami in the northern Bungo Channel.

We use this new and independent constraint to re-examine the validity of the Hōei earthquake source models by Furumura et al. (2011) and Hyodo and Hori (2013) by

simulating tsunami runup on a high-resolution bathymetric grid around Lake Ryuuoo. Both earthquake sources are unable to produce a tsunami that inundates Lake Ryuuoo, indicating that they are inconsistent with sedimentological evidence of the 1707 tsunami. We then test a series of new, observation-based rupture scenarios by making the assumption that coseismic slip follows present-day patterns of geodetically imaged interseismic coupling estimated by Loveless and Meade (2010). These coupling-based scenarios generate a tsunami that better matches both historical and sedimentological observations in southwestern Japan, suggesting that spatial trends in present-day coupling models may be consistent with past periods of coseismic rupture along the Nankai Trough.

TABLE OF CONTENTS

LIST OF TABLES

LIST OF FIGURES

CHAPTER 1

SEDIMENTOLOGICAL RECORDS OF THE C.E. 1707 HŌEI TSUNAMI AND REGIONAL COASTAL FLOODING FROM THE BUNGO CHANNEL, SOUTHWESTERN JAPAN

1.1 Abstract

A tsunami generated by the C.E. 1707 Hōei earthquake is largely thought to be the flood event of record for southwestern Japan, yet historical documentation of the event is scarce. This is particularly true in northwestern Shikoku within the Bungo Channel, where significant inconsistencies exist between historical records and model-derived tsunami heights. To independently assess flooding from the C.E. 1707 Hōei tsunami in the context of the region's long-term flooding history, we present complementary reconstructions of extreme coastal inundation from three back-barrier lakes in the northern Bungo Channel: Lake Ryuuoo, Lake Amida, and Lake Kamega. At all sites, the most prominent marine overwash deposit of the past ~1,000 years, as defined by grain size, density, and geochemical indicators, is consistent with the timing of the 1707 tsunami, providing strong evidence that the event caused the most significant flooding of the last millennium in this region. At Lake Ryuuoo, modern barrier beach elevations and grain sizes in the tsunami's resultant deposit provide ~4 m as the first physically based height constraint for the 1707 tsunami in the northern Bungo Channel.

Around 1,000 years ago, a concurrent and abrupt transition in lithology observed at all three sites is also consistent with rapid, regional geomorphic change. At Lake Ryuuoo, a marine overwash deposit comparable to the 1707 deposit directly overlies this transition. A

1,000-year-old lithological transition or deposit has not been observed at sites closer to the mouth of the Bungo Channel, suggesting that the deposit in Lake Ryuuoo is more consistent with a tsunami generated by local seismicity along the Japan Median Tectonic Line than with a Nankai Trough-derived tsunami. Our findings are significant in that they provide three new millennial-scale tsunami inundation reconstructions for a relatively understudied region of Japan, along with the first physically based height constraint for the Hōei tsunami in the northern Bungo Channel.

1.2 Introduction

The 2011 Tōhoku earthquake and tsunami exposed the limitations of relying on a temporally limited instrumental record for assessing earthquake and tsunami hazards (e.g. Goto et al., 2011). In response, recent studies have demonstrated the value in using longer-term historical and geologic reconstructions of extreme flooding to improve current risk assessments of tsunami inundation (e.g. Sugawara et al., 2011; Goto et al., 2012; Chagué-Goff et al., 2012). Specifically, marine overwash event deposits preserved within the sediments of coastal back-barrier lakes can provide an opportunity to independently assess past periods of extreme flooding in tsunami prone areas (e.g. Nanayama et al., 2002; Okamura et al., 2004).

Like northern Japan, southwestern Japan has a long documented history of tsunami occurrences. Megathrust earthquakes are estimated to occur every 100 to 200 years off the region's Pacific coast along the Nankai Trough (Fig. 1.1), where the Philippine Sea Plate obliquely subducts to the northwest beneath the Eurasia Plate (Ando, 1975; Ishibashi, 2004). The only Nankai Trough-derived tsunami to impact southwestern Japan over the recent

instrumental record occurred in C.E. 1964; however, early historical accounts provide documentation for at least eight additional tsunami impacts to the region over the last 1,500 yrs in C.E. 1854, 1707, 1605, 1498, 1361, 1099, 887, and 684 (Ishibashi, 2002).

Northwest of the Nankai Trough, intraplate seismicity capable of tsunamigenesis poses an additional flooding risk to southwestern Japan. Specifically, stresses imposed by oblique subduction offshore generate shallow inland earthquakes along the Japan Median Tectonic Line (Fig. 1.1), a 300 km long right-lateral strike-slip fault that bisects southwestern Japan (Fitch, 1972). In Shikoku, the Median Tectonic Line has a late Quaternary slip rate of 5-10 mm/yr (Okada, 1973, 1980) and is thought to rupture in segments every 1000-3000 yrs with surficial offsets of 5-8 m (Tsutsumi and Okada, 1996). The historically recorded C.E. 1596 Keicho-Bungo earthquake represents an instance where submarine faults in Beppu Bay, located ~40 km west of the Sadamisaki Peninsula (Fig. 1.1), likely ruptured simultaneously with parts of the Median Tectonic Line to generate a destructive tsunami with observed wave heights up to 8 m along Beppu Bay's coast (Ishibe and Shimazaki, 2005; Hatori, 1985).

Among the earthquakes and tsunamis documented in southwestern Japan, the C.E. 1707 Hōei Nankai megathrust earthquake is widely thought to have resulted in the tsunami event of record for the region. It likely ruptured the entire length of the trough and is often referred to as the worst-case scenario for a Nankai megathrust event (e.g. Furumura et al., 2011). Recent estimates for its magnitude exceed M_W 9 (e.g. Hyodo and Hori, 2013), and the resulting tsunami caused damage throughout southwestern Honshu, Shikoku, and southeastern Kyushu, with documented inundation heights reaching 10 m in the most severely impacted areas (Murakami et al., 1995 and references therein). Constraining flooding conditions during the event is therefore key to tsunami risk-assessment in

southwestern Japan; however, solely relying on historical records is insufficient, in part because observations of the event are relatively scarce in terms of their temporal and spatial coverage, and historical seismologists have cited significant uncertainties related to their reliability (Ishibashi, 2004; Ando, 1975; Murakami et al., 1995).

Recently, Furumura et al. (2011) and Hyodo et al. (2014) have run tsunami simulations for Hōei earthquake source models to compare the maximum model-derived tsunami heights to historical observations. Both studies found earthquake scenarios that yielded good agreement between modeled and observed tsunami heights along the open Pacific coastlines of Shikoku and Honshu, but those same scenarios also under-predicted tsunami heights in the northern Bungo Channel and Seto Inland Sea by as much as 3 m (Fig. 1.1). Specifically, limited historical documentation of the Hōei event describes a 5-m tsunami in the northwestern Shikoku villages of Uwajima and Yoshoda (locations E and F in Fig. 1.1) (Murakami et al., 1995) and a 1 – 3 m tsunami in the Seto Inland Sea (Hatori, 1988), that simulations by Furumura et al. (2011) and Hyodo et al. (2014) were unable to reproduce. This is a particularly important area for accurate flood hazard assessment because many forms of sensitive and critical infrastructure are present along the shore of the Bungo Channel. Among them is the sole nuclear power plant for the island of Shikoku (location G in Fig. 1.1), which is located on the Sadamisaki Peninsula, a prominent peninsula that extends into the channel (Fig. 1.1).

In summary, the C.E. 1707 Hōei event is thought by many to have caused the largest and most destructive historical Nankai tsunami (e.g. Furumura et al., 2011), yet significant discrepancies exist between observational accounts and recent tsunami simulations in a key risk assessment region for southwestern Japan. Here, we aim to reduce this uncertainty using

three new lacustrine sedimentary reconstructions of coastal inundation in the Bungo Channel that provide an independent evaluation for the severity of the 1707 tsunami relative to other extreme flooding events impacting the region over the last millennium.

1.3 Field Sites

Lake Ryuuoo, Lake Amida, and Lake Kamega lie along the northeastern coast of the Bungo Channel on or near the Sadamisaki Peninsula, and they are well situated to record Nankai Trough-derived tsunami events (Fig. 1.1). The three lakes lie behind relatively short sand and cobble barrier beaches that are secured between adjacent steep, rocky headlands (Fig. 1.1). Barrier beaches with similar morphologies along the southwestern coast of Japan have remained relatively stable in their configurations over the last few millennia of modest relative sea level change (Woodruff et al., 2009, 2013, 2015). The Median Tectonic Line and parallel lineaments also run along the northern side of the Sadamisaki Peninsula, some of which are active Quaternary faults (Fig. 1.1) (Okada, 1973, 1980; Research Group for Active Faults of Japan, 1991). Thus, local tectonics may have caused more rapid changes in relative sea level around the Sadamisaki Peninsula in the past; however, lower frequency changes due to glacial-isostatic components are relatively low, with prior estimates equaling ~0.2 – 0.7 mm/yr of steady sea-level rise over the past 6,000 years around the peninsula (Nakada et al., 1991).

1.3.1 Lake Ryuuoo

Of the three sites, Lake Ryuuoo has the smallest barrier (3.1 – 3.8 m above mean sea level (MSL), ~40 m wide, and ~200 m long) and is therefore likely the most sensitive

recorder of overwash. The lake has a maximum depth of 2 m and a surface area of 18,000 m^2. It is also the most pristine of the three study sites, as it lies on the coast of Jio Island (Fig. 1.1), which currently has no permanent residents. Residents from the island to the north have only made minor modifications to the site, which include the building of a ~2 m high sea wall along its barrier in 1964 (Oshima District town hall, 2008), a jetty offshore in 1980 (H. Shibanaka, Ehime Prefecture official, personal communication, February 14, 2014), and an underground pipe connecting Lake Ryuuoo to the ocean within the past ~70 years (K. Hyodo, Oshima town hall director, personal communication, July 23, 2014).

1.3.2 Lake Amida

Lake Amida is larger than Lake Ryuuoo and located on the southern side of a major embayment along the western tip of the Sadamisaki Peninsula (Fig. 1.1). The lake has a substantial barrier (2.9 – 4.1 m above MSL, ~150 m wide, and ~350 m long), a maximum depth of 7 m, and a surface area of 54,000 m^2. Two small streams inflow to the lake from the south and northeast, with a total watershed area of 0.6 km^2. The area remained relatively pristine until the last century, when the barrier was populated, a series of seawall and jetty fortifications was constructed in 1996 (M. Ushio, Ikata town official, personal communication, March 18, 2006), and a channel was constructed through the lake's barrier to allow for freshwater drainage of the lake to the ocean. Orange groves are also abundant on the surrounding hillslopes, and results from Kanai and Inouchi (2004) indicate a rapid increase in sedimentation rates in Lake Amida concurrent with land clearance for these orchards in the late 1800s.

1.3.3 Lake Kamega

Lake Kamega is located on the southern side of the Sadamisaki Peninsula. Similar to Lake Amida, Kamega has a large, currently developed barrier (3.5 – 4.8 m above MSL, ~130 m wide, and ~300 m long) (Fig. 1.1). The lake has a maximum depth of 7 m and surface area of 96,000 m^2, and a larger stream inflows to the lake from the west with a total watershed area of 1.4 km^2. Kanai and Inouchi (2004) observed relatively steady and modest rates of sedimentation in Lake Kamega until the 1950s, after which increased rates of deposition were linked to land clearance for orange orchards and more significant modifications to the barrier, including the construction of a channel through the lake's barrier that now allows for controlled freshwater drainage of the lake to the ocean.

1.4 Methods

1.4.1 Field methods

An initial geophysical survey of the lakes using a 10 kHz sub-bottom sonar was used to map each site's bathymetry, assess sub-bottom stratigraphy, and identify sediment core target locations. Acoustic ringing due to Lake Ryuuoo's shallow depths prevented the acquisition of sub-bottom sonar but still allowed for a bathymetric assessment. In Lake Amida and Lake Kamega, gas in sub-bottom sediment often attenuated the sonar signal; however, areas where the signal was not attenuated revealed surficial units of continuous, parallel, acoustically laminated sediment without any major erosional unconformities. Primary sediment cores were collected from the deepest section of each lake using a modified Vohnout-Colinvaux piston corer (Donnelly and Woodruff, 2007). Discrete surface samples were also collected from barrier beaches, freshwater tributaries, and bedrock

outcrops at the three sites to identify and delineate characteristics of allochthonous sediment. Following collection, all cores were shipped back to the University of Massachusetts (Amherst, USA) and stored under 4 °C refrigeration.

1.4.2 Non-destructive analyses

All cores were split, described, and photographed. Working core halves were first run on a non-destructive Itrax X-ray fluorescence (XRF) scanner (Croudace et al., 2006) to detect variability in relative abundances of bromine (Br), strontium (Sr), and Sr relative to titanium (Sr/Ti). Br counts are commonly used to estimate marine organic carbon content and paleosalinity in sediment cores (Ziegler et al., 2008; Mayer et al., 1981, 2007). Sr is found in high concentrations within the marine-sourced shell, coral, and algal material that is often advected into back-barrier lakes during periods of coastal flooding (e.g. Bowen, 1956; Woodruff et al., 2008, 2009, 2015). Finally, Ti is widely used as a proxy for terrestrially derived clastic material (Peterson et al., 2000; Shanahan et al., 2008; Kirwan et al., 2011). Here, we use the ratio of Sr/Ti both to serve as a proxy for the relative abundance of marine versus terrigenous material in the core, and to help illuminate any potential single-element biasing due to changes in sediment density or grain size (e.g. Croudace et al., 2006; Vlag et al., 2004; Bahr et al., 2005).

In order to assess the effectiveness of Sr/Ti as a proxy for marine versus terrigenous material in the cores, discrete surface samples were also run on the Itrax core scanner to evaluate the relative abundances of Sr and Ti in sediment from different sources. Barrier beach sediments from Lake Ryuuoo and Lake Kamega were sieved at 125 μm prior to scanning in order to gain separate Sr/Ti counts for silt to very fine sand and for medium to

coarse sand. Barrier beach sediment from the currently fortified beach at Lake Amida was almost entirely >125 μm, so it was not sieved before scanning.

Magnetic susceptibility (MS) and relative density measurements using digital X-ray radiography were also obtained for the core halves from the Itrax core scanner. The x-radiographs revealed density variations in the cores, where anomalously dense bands have been effectively used as a proxy for event-driven deposition (e.g. Boldt et al., 2010; Brandon et al., 2014; Woodruff et al., 2015). Peaks in MS often indicate the presence of denser ferromagnetic or paramagnetic minerals commonly found on beaches and concentrated within high-energy event layers (e.g. Buynevich, 2011).

1.4.3 Discrete sample analyses

Organic content in sediment was quantified based on the percent weight loss-on-ignition (LOI), following methods described by Dean (1974). Event beds are commonly identifiable by peaks in inorganic content, expressed as 100 minus the percent LOI (e.g. Scileppi and Donnelly, 2007; Liu and Fearn, 1993, 2000; Woodruff et al., 2015).

Event deposits were identified with a multi-proxy approach by locating anomalously dense horizons in the x-radiograph that corresponded with peaks in Sr/Ti, MS, and percent clastic material. Following identification, individual event deposits were sub-sampled at 1 cm depth intervals for further grain size analysis. Grain size analysis was only performed for the Lake Ryuuoo core, as this site is the most sensitive to overwash and therefore had the most easily identifiable deposits. Grain size subsamples were wet sieved with a 32 μm sieve and reacted with 6% hydrogen peroxide to remove organic material. Here we define coarseness as percent >32 μm, which roughly represents the transition between medium and

coarse silt. Measurements of coarseness were obtained based on the dry weight of inorganic material retained in the 32 μm sieve relative to the total dry bulk weight of the sample before sieving. Grain size of the clastic, coarse, sieved fraction was measured using a Coulter LS 200 laser particle analyzer, and measured distributions were adjusted for the percent of sediment finer than 32 μm (e.g. Brandon et al., 2014). The D_{95} grain size is presented for the most prominent deposits, where D_{95} defines the grain size that 95% of the sample is finer than and is assumed to be representative of the coarsest grains in a sample (Woodruff et al., 2008).

1.4.4 Core chronology

Depth-to-age conversions for each core were based on ^{137}Cs and ^{14}C chronologies. A Canberra GL2020R Low Energy Germanium Detector identified the onset and subsequent peak in ^{137}Cs, marking the C.E. 1954 beginning and C.E. 1963 peak in atmospheric nuclear testing, respectively (Pennington et al., 1973). For these analyses, approximately 2.0 g of powdered sediment was counted on the detector for 24 – 48 hrs, and activities for ^{137}Cs were computed spectroscopically from the 661.7 keV photopeak. Eighteen Accelerator Mass Spectrometry (AMS) ^{14}C dates of terrestrial, organic macrofossils (leaves and small twigs) were used to date sediment prior to the last century (Tab. 1.1). Samples were dated at the National Ocean Sciences Accelerator Mass Spectrometry Facility (NOSAMS) in Woods Hole, MA, the Keck Carbon Cycle AMS Facility at University of California-Irvine, and Chikyu Kagaku in Nagoya, Japan. Radiocarbon ages were converted to calendar years before C.E. 1950 (yrs BP) using IntCal13 (Reimer et al., 2013). Bayesian depth-to-age models were generated for the three sites using the Bchronology function in the Bchron R

package and ^{137}Cs and ^{14}C age constraints (Haslett and Parnell, 2008; Parnell et al., 2008). Ages of overwash deposits were determined by averaging the model-generated posterior ages at 1 cm intervals through the deposits. We present model-generated ages assigned to depths between age controls using the 95% highest posterior density region (HDR) and rounding ages to the nearest 10 yrs to avoid false precision.

1.5 Results

1.5.1 Lake Ryuuoo sediment

Fig. 1.2 shows results for the primary core (RYU1, see Fig. 1.1 for location) and discrete surface samples from Lake Ryuuoo. The RYU1 core extended 934 cm below the sediment-water interface, capturing a ~2,500 year long record of deposition in the lake. A finely laminated (mm-scale) unit of very fine-grained sediment extended from the base of the core upward to a sediment depth of 595 cm. This unit was followed by a visually distinct change in lithology to homogenous gyttja interbedded with coarse-grained deposits. Percent clastic material and MS abruptly increased within this gyttja unit (Figs. 1.2c and 1.2f), and the elemental abundance of Br decreased (Fig. 1.2d). Radiocarbon ages just above and below the transition at 595 cm provided a 95% HDR of C.E. 1020 – 1120 (median = C.E. 1060).

Between the 595 cm transition and 100 cm, there were ten distinct coarse-grained deposits. These deposits were defined as anomalously dense, cm-scale layers with coarse fractions that exceed 15% coarse (Fig. 1.2e). Deposits also exhibited concurrent peaks in percent clastics, MS, and Sr/Ti (Figs. 1.2c, 1.2f, 1.2g). Peaks in Sr/Ti were consistent the deposits being marine-sourced, as discrete barrier beach samples exhibited Sr/Ti ratios 7 – 8

times greater than terrigenous sediment from surrounding hillslopes did (Fig. 1.2i). A coarse-grained deposit directly above the lithological transition at 595 cm (88% coarse, 19 cm thick, D_{95}=430 μm) and a deposit at 271 cm (76% coarse, 25 cm thick, D_{95}=225 μm) were the two most prominent coarse-grained layers within the RYU1 sedimentary sequence. Model-derived 95% HDRs for the deposits at 595 cm and 271 cm were C.E. 1030 – C.E. 1130 and C.E. 1700 – C.E. 1780, respectively (Fig. 1.2h).

Between 100 cm and the sediment-water interface, RYU1 displayed a rapid drop in density, percent clastic material, MS, and Sr/Ti (Figs. 1.2b, 1.2c, 1.2f, and 1.2g). No coarse-grained layers were evident in this top 100 cm section of the core (Fig. 1.2e). The onset of ^{137}Cs and the uppermost ^{14}C age constrained the depth-to-age model to provide a 95% HDR of C.E. 1830 – C.E. 1950 for the onset of this transition at 100 cm (Fig. 1.2h).

1.5.2 Lake Amida sediment

Core AMI2, taken from Lake Amida's primary core site (Fig. 1.1), extended 500 cm below the sediment-water interface, with a radiocarbon age at 493 cm that indicated a total record length of ~2,500 years (Fig. 1.3g and index #12 in Tab. 1.1). AMI2 was mostly composed of homogenous gyttja with occasional light gray clay layers (Fig. 1.3a, and unlike RYU1, it did not contain any coarse sediment. ^{137}Cs and ^{14}C dates were both consistent with a dramatic increase in average sedimentation rates from 0.1 cm/yr for sediment between the base of the core (526 cm) and 250 cm, to 0.9 cm/yr for sediment between 250 cm and the sediment-water interface. The core's depth-to-age model provided a 95% HDR of C.E. 1670 – C.E. 1850 for the onset of this increased rate (Fig. 1.3g). Sedimentation rates were

calculated using model-derived mean ages at 526 cm and 250 cm and the year that the core was collected (C.E. 2010) at the sediment-water interface.

Sedimentary trends from AMI2 were generally consistent with those noted in Lake Ryuuoo. The core contained a lower unit with low percent clastics and MS but high Br counts, followed by a transition at 330 cm to sediment with higher percent clastics and MS, but substantially lower Br abundance (Figs. 1.3c – 1.3e). The depth-to-age model provided a 95% HDR of C.E. 650 – C.E. 1260 at this 330 cm transition (Fig. 1.3g). The most prominent dense deposit in the AMI2 x-radiograph was observed above the transition at a sediment depth of 270 cm and was accompanied by a dominant peak in MS (Fig. 1.3e). Sr counts also nearly doubled in this layer, but a peak in Sr/Ti was not evident due to an equally large peak in Ti (Fig. 1.3f). The depth-to-age model provided a 95% HDR of C.E. 1500 – C.E. 1740 for the deposit (Fig. 1.3g). The largest peak in Sr/Ti occurred at 33 cm and was accompanied by a peak in percent clastic material (Figs. 1.3f and 1.3c). This 33 cm depth was above the C.E. 1963 peak in Cs-137, with the core's depth-to-age model providing a mean age of C.E. 1993 at 33 cm.

Lake Amida's currently fortified barrier beach only contained sediment >125 μm, so Sr/Ti could only be measured for marine sediment that was coarser than the material observed in core AMI2. This coarse-grained barrier beach sediment yielded a Sr/Ti ratio ~5 times greater than that of proximal terrigenous sediment (Fig. 1.3i).

1.5.3 Lake Kamega sediment

KAM2 was taken from Lake Kamega's primary core site (Fig. 1.1). The core extended 689 cm below the sediment-water interface, with a mean radiocarbon age at 689 cm

of 3313 yrs BP (Fig. 1.4 and index #18 in Tab. 1.1). Between the base of the core and 385 cm, sediment was very fine-grained and gray in color, with abundant mm-scale laminations and four ~1 cm thick sandy layers at 473, 529, 533, and 557 cm (Fig. 1.4a). A visually distinct change in lithology occurred at 385 cm. The change was similar to that observed in sediment from Lake Ryuuoo and Lake Amida in that it was accompanied by an increase in MS and percent clastic material (Figs. 1.4e and 1.4c) and a decrease in the elemental abundance of Br (Fig. 1.4d). The depth-to-age model provided a 95% HDR of C.E. 960 – C.E. 1450 for this transition at 385 cm.

Sediment above the transition was homogenous gyttja and only contained one visually distinct gray clay layer at 216 cm (Fig. 1.4a), with a 95% HDR age range of C.E. 1700 – 1900 (Fig. 1.4g). The deposit appeared very dense in the X-radiograph (Fig. 1.4b) but only corresponded with weak peaks in MS and Sr/Ti (Figs. 1.4e and 1.4f). However, there was also almost no detectable difference in Sr/Ti between fine-grained barrier beach sediment and fluvial sediment from Lake Kamega (Fig. 1.4h), suggesting that Sr/Ti ratios are less indicative of barrier/marine-derived sedimentation at the site. Marine flood deposits commonly thin in the landward direction (Minoura et al., 1997; Chagué-Goff et al., 2002; Donnelly et al., 2004; Woodruff et al., 2008, 2015; Brandon et al., 2014), so due to the subtleness of the event layer in KAM2, X-radiographs of two additional sediment cores from Lake Kamega were analyzed to assess spatial variation in the deposit's thickness. Using the lower transition in lithology as a stratigraphic constraint in each core, the deposit could be traced landward and appeared to thin from 16 cm near the barrier in KAM2, to 10 cm in the middle of the lake in KAM4, to barely distinguishable near the lake's landward shore in KAM3 (Fig. 1.5).

1.6 Discussion

1.6.1 C.E. 1707 Hōei tsunami deposit

The timing for the most prominent event deposit over the last ~1,000 years of relatively uniform lithology is consistent with the 1707 tsunami at all three study sites. Radiocarbon uncertainties preclude an exact matching of the deposits to the Hōei event, but Japan's historical records provide additional evidence that the two are linked. In Fig. 6, the age distribution for the most prominent event deposit at each of the three study sites is plotted alongside major Nankai Trough earthquakes documented for southwestern Japan between the 9th century and C.E. 1990 (Ishibashi, 2002). Among these events, the 1707 tsunami is the only major Nankai Trough event that consistently falls within the 95% HDRs of the model-generated posterior ages for deposits at all the three lakes. Typhoons present an alternative mechanism for deposit formation (e.g. Woodruff et al., 2015); however, a town hall record from Jio Island that documents tsunami and typhoon impacts to the island since C.E. 1656 mentions only the C.E. 1707 tsunami when discussing notable flooding events impacting the island between the late 17th and early 18th centuries. Therefore, although there is currently no way to unequivocally distinguish typhoon and tsunami deposits, in the case of the Hōei event, historical documentation of the tsunami and the temporal and regional coherency of the overwash deposit combine to provide strong evidence that this observed deposit is of tsunamigenic origin.

Depositional characteristics of the early 18th century deposits at the three study sites also support high-energy marine flooding as the most likely mechanism of formation. This is most evident at Lake Ryuuoo, where concurrent peaks in density, MS, percent clastics, and

grain size are consistent with high energy, event-driven deposition (e.g. Goff et al., 2012; Brandon et al., 2014). Furthermore, peaks in Sr and Sr/Ti, when placed in the context of the surficial sediment analysis presented in Fig. 2i, are consistent with the barrier beach as a sediment source for event deposits in the Ryuuoo core.

The fine-grained event deposits observed in Lake Amida and Lake Kamega are subtler. These two sites likely do not contain sandy deposits because they are much larger systems than Lake Ryuuoo, both in terms of lake and barrier size. Sand-sized sediment is present on their barriers, but an inundating flow may only have had the transport competency to suspend and advect clay and silt after traveling such large distances over their barriers to the lakes. This explanation is supported by observations on the Sendai Plain following the 2011 Tōhoku tsunami, where a significant portion of areas inundated experienced predominantly mud deposition rather than sand deposition (Chagué-Goff et al., 2012). A weaker Sr/Ti signature is also observed for the early 18th century deposits at Lake Amida and Lake Kamega. For Lake Kamega, this finding is consistent with the surficial sediment XRF results, which show that the Sr/Ti signature of fine-grained barrier beach sediment (<125 μm) is hardly distinguishable from the Sr/Ti signature of terrigenous and fluvial sediment (Fig. 4h). However, the observed landward thinning trend of the deposit (Fig. 5) provides evidence that the layer was deposited while sediment was being advected landward and settling out of suspension during a marine inundation of the barrier (Minoura et al., 1997; Chagué-Goff et al., 2002; Donnelly et al., 2004; Woodruff et al., 2008, 2015; Brandon et al., 2014). Barrier beach material collected from Lake Amida was entirely coarser than 125 μm, likely due to heavy modification of the barrier with coastal structures, so the Sr/Ti signature of fine-grained material could not be assessed. Aside from the peak in MS associated with

the lake's early 18th century deposit, there is no other evidence to distinguish its source as marine versus terrigenous; however, the deposit's temporal consistency with the most sedimentologically prominent event layers at Lake Ryuuoo and Lake Kamega, as well as its correlation to the documented flood event of record for the region in C.E. 1707, provides strong evidence that it is also linked to the Hōei event.

1.6.2 Tsunami versus storm deposition

Western Shikoku is prone to coastal flooding by typhoons in addition to tsunamis. The instrumental record from the Joint Typhoon Warning Center (JTWC) best track data set extends back to C.E. 1945 and contains four typhoons passing within 70 km of Lake Ryuuoo (i.e. maximum sustained winds in excess of 118 km/hr, or 63 knots) (Chu et al., 2002), but with none exceeding Category 2 intensity (>96 knot winds). Of the three sites, Lake Amida was the only one that potentially contained a modern event deposit. In the AMI2 core, peaks in clastic material and Sr/Ti were observed at 33 cm (Figs. 1.3c and 1.3f), well above the C.E. 1963 peak in ^{137}Cs. According to the JTWC instrumental record, the most severe typhoon impact within the best track instrumental dataset occurred in C.E. 1990 when Typhoon Zola made landfall on the eastern end of the Sadamisaki Peninsula at Category 2 intensity, consistent with the timing of the event layer at 33 cm in Lake Amida.

There is currently no means to unequivocally distinguish tsunami and storm deposits. It is particularly challenging in Japan, as recent coastal fortifications have prevented the formation and preservation of typhoon deposits that can be used as modern analogues for comparison to deposits that predate the instrumental record. Sediments in Lake Ryuuoo, Lake Amida, and Lake Kamega all reveal changes in their depositional environments in

modern times. For example, the increase in organic sediment and the lack of coarse material in the upper meter of RYU1 is likely a result of sea wall and jetty construction, and the increase in Sr/Ti in the upper sections of the cores from all three sites is likely associated with the building of inlets or culverts through their barriers.

In the case of the C.E. 1707 Hōei event, historical records provide abundant evidence for a tsunami impacting southwestern Japan (e.g. Ishibashi, 2002; Murakami et al., 1995; Oshima District town hall, 2008), while Jio Island town hall records do not document a major typhoon event in the early 18th century. These historical accounts, when combined with the presence of a temporally and regionally coherent overwash deposit in northwestern Shikoku that dates to the early 18th century, provide strong evidence for the prominent deposits at Lake Ryuuoo, Lake Amida, and Lake Kamega being associated with the Hōei tsunami.

1.6.3 C.E. 1707 Hōei tsunami height constraints

The C.E. 1707 event layer at Lake Ryuuoo contains the coarsest sand grains of all nine event deposits within the upper ~590 cm of uniform lithology in RYU1 (i.e. excluding the deposit immediately overlying the lithological transition at 595 cm). In previous studies, grain size has been found to be one of the best proxies for flood magnitude (e.g. Jaffe and Gelfenbaum, 2007; Jaffe et al., 2012; Woodruff et al., 2008; Brandon et al., 2013, 2014). Findings at Lake Ryuuoo are therefore consistent with the C.E. 1707 tsunami representing the most extreme flooding event to impact the northern Bungo Channel over the last ~1,000 years.

The advective settling model, illustrated in Fig. 1.7a, provides a well-tested relationship between the flow depth over a barrier beach of an inundating wave and the

maximum settling velocity for grains in a resulting back-barrier deposit (e.g. Moore et al., 2007; Woodruff et al., 2008; Wallace et al., 2014; Brandon et al., 2014). Once the tsunami overtops the barrier and reaches the lake, the model assumes that the time t it takes for the inundating flow with an average flow speed U_L to transport a grain a horizontal distance x_L from the barrier to its final resting place in the lake is equal to the time it takes that same grain with settling velocity w_s to settle the vertical distance h_L from the surface of the flow to the lake's bed, such that:

$$t = \frac{x_L}{U_L} = \frac{h_L}{w_s} \tag{4}$$

This basic assumption requires that sediment in the water column is fully mixed at the barrier and subsequently transported in suspension, and it requires that during overwash, grain sizes are laterally sorted through the lake such that larger grains with faster settling velocities are deposited seaward of smaller grains with slower settling velocities. The C.E. 1707 deposit in Lake Ryuuoo exhibits lateral sorting trends that support this assumption. Percent coarse measurements of the C.E. 1707 deposit in a transect of cores perpendicular to the barrier, where RYU1 is closest to the barrier, and RYU4 and RYU3 are progressively farther inland, show that the amount of sediment coarser than 32 μm in the C.E. 1707 deposit is greatest near the barrier and decreases landward (Fig. 1.8).

Next, conservation of mass requires that volumetric flow rate Q is the same over the barrier and in the lake, such that:

$$\mathrm{Q} = U_L h_L = f U_b h_b \tag{5}$$

where U_b and h_b are average flow velocity and flow depth over the barrier (Fig. 1.7a), and f is the ratio of flow width over the barrier to flow width in the lake. The elevation of the barrier varies, so f roughly accounts for the fact that when the flood elevation is between the

minimum and maximum barrier height, only a fraction of the barrier is inundated, such that the flow will become wider, shallower, and slower when it enters the lake.

We can then use the Froude number to relate flow velocity and flow depth, yielding the relationship:

$$U_L h_L = f U_b h_b = f * Fr_b * \sqrt{g h_b{}^3} \quad (6)$$

where Fr_b is the Froude number over the barrier, and g is the acceleration due to gravity (Woodruff et al., 2008). Finally, combining Eq. 6 with Eq. 4 gives a unique solution for the maximum grain size (which is related to settling velocity) that a given flow depth h_b is able to transport a horizontal distance x_L from the barrier for an assumed Froude number:

$$w_s = \frac{f * Fr_b * \sqrt{g h_b{}^3}}{x_L} \quad (7)$$

At Lake Ryuuoo, flow likely would have been greatest over the low-elevation region of the barrier, so we apply Eq. 7 to a particle being transported a horizontal distance of 100 m from this low region to the location of RYU1. Field and experimental observations have also indicated that during overwash, the inundating flow transitions to supercritical along the backside of the barrier (Donnelly et all, 2006; Holland et al., 1991), so we vary Fr_b between 0.8 and 1.5 in Eq. 7.

Fig. 1.7b shows the resulting relationship between maximum settling velocity w_s and flow depth h_b over the low region of the barrier. Following Woodruff et al. (2008), we use D_{95} to represent the maximum grain size observed in the RYU1 deposit, and we calculate settling velocity for this grain size using the relationship developed by Ferguson and Church (2004). D_{95} for the coarsest interval of the C.E. 1707 deposit in RYU1 is 225 μm and has a settling velocity of 0.015 m/s. Using the relationship in Fig. 1.7b a constrained range of 0.6 –

0.7 m is obtained for the 1707 tsunami's flow depth over the low-elevation region of the barrier.

Combining this calculation with the 3.1 m minimum elevation of Lake Ryuuoo's barrier beach provides a height estimate of roughly 4 m for the 1707 tsunami around Lake Ryuuoo. The 1707 earthquake likely caused some amount of coseismic subsidence around Jio Island (e.g. Furumura et al., 2011; Hyodo et al., 2014), so we define tsunami height as the distance between the ocean surface following coseismic deformation and the crest of the tsunami. This estimate also assumes relatively consistent barrier beach height over the last 300 yrs, which is reasonable given that coseismic surface deformation is usually resolved to a normal level over tens of years following an earthquake (e.g. Furumura et al., 2011) and that Lake Ryuuoo's barrier beach has a stable configuration between two protruding headlands in a region with relatively low rates of sea-level rise and limited anthropogenic modifications.

1.6.4 Change in lithology

The concurrent and abrupt lithological change observed at all three study sites around CE. 1000 suggests a sudden and significant alteration to barrier environments throughout the Sadamisaki Peninsula region. The coarse-grained event deposit immediately overlying the transition in Lake Ryuuoo also indicates that the environmental change was associated with a high-energy flood event. Depositional evidence for contemporaneous high-energy inundation and rapid coastal geomorphologic change has been linked to tectonic subsidence and associated tsunami generation (e.g. Atwater, 2005; Peters et al., 2007; Wright and Mella, 1963).

Seismicity along the Median Tectonic Line (MTL) (Fig. 1.1), which bisects southwestern Japan and runs along the Sadamisaki Peninsula, is consistent with seismically induced geomorphic change focused primarily around our study area. Stresses imposed by oblique subduction offshore along the Nankai Trough generate shallow inland earthquakes along the MTL. Although there are no historical documents suggesting destructive MTL earthquakes for at least the past 1000 yrs (Usami, 1987), modern geologic studies aimed at reconstructing Holocene surface faulting have found that small segments of it rupture every 1000 – 3000 yrs, with large horizontal surface displacements of up to 8 m (Tsutsumi and Okada, 1996; Okada, 1973, 1980; Research Group for Active Faults of Japan, 1991). Rupture along the MTL therefore appears to be a viable cause for the sudden transition in lithology and associated tsunami deposit for sites in the Sadamisaki Peninsula region.

There is some limited documentation for a Nankai megathrust earthquake and tsunami occurring in C.E. 1099, so it is possible that this ~1000 yr-old deposit resulted from a remotely generated Nankai tsunami. However, toward the mouth of the Bungo Channel, a previously developed lacustrine record of Nankai Trough-derived tsunamis from Lake Ryujin (location D in Fig. 1.1) does not contain evidence for a tsunami event or display a lithological change around 1000 yrs ago (Okamura et al., 2004). Furthermore, the rapid geomorphic change that accompanies the event deposit overlying the lithological transition in Lake Ryuuoo distinguishes it from all other deposits in the record, including the 1707 Nankai Trough-derived tsunami deposit. The uniqueness of the C.E. 1000 deposit compared to all other event deposits in the record is therefore consistent with an alternative mechanism for tsunami generation.

1.7 Conclusions

We present three millennial-scale records of coastal flooding from back-barrier lakes within the Bungo Channel in southwestern Japan. Within the last ~1,000 years of uniform lithology at all three sites, the timing of the most prominent marine overwash deposit is consistent with the C.E. 1707 Hōei event and supports the resultant tsunami being the most significant flood event to impact the Bungo Channel during this time period. Although there is currently no way to unequivocally distinguish typhoon and tsunami deposits, in the case of the Hōei event, historical documentation of the tsunami and the temporal and regional coherency of the overwash deposit combine to provide strong evidence that this observed deposit is of tsunamigenic origin. We also use the grain size of the C.E. 1707 tsunami deposit in Lake Ryuuoo, along with modern elevations of its barrier beach, to provide a height estimate of ~4 m for the Hōei tsunami at Jio Island.

A concurrent change in lithology also occurs at all three sites around C.E. 1000. Sedimentological evidence of geomorphic change and the occurrence of a significant marine flooding event immediately following the lithological transition points to regional seismicity as a viable mechanism for this change. When considering flood hazards to northwestern Shikoku, results presented here provide support for both Nankai Trough-derived tsunamis, and tsunamis generated by local seismicity as significant regional hazards.

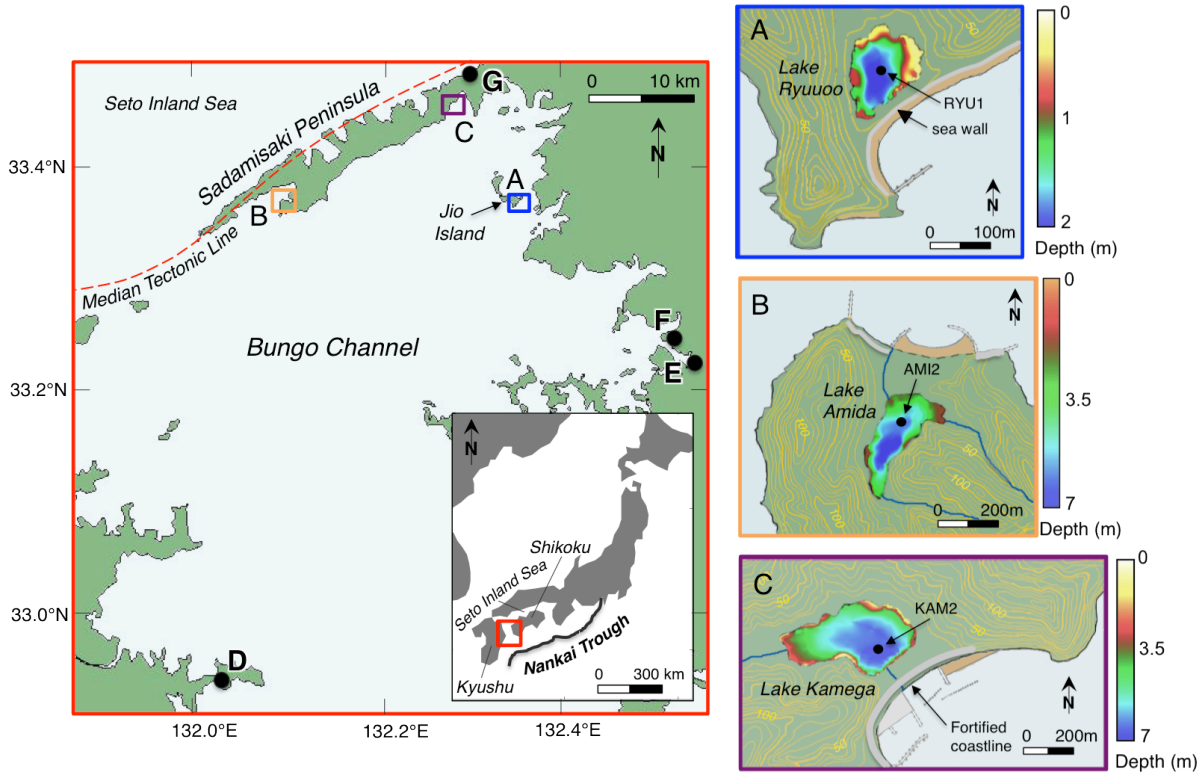

Figure 1.1. Regional setting and study site map. (Left) Regional map of the northern Bungo Channel showing study sites (A, B, and C) and other locations mentioned in the text, including a previous tsunami reconstruction from Lake Ryujin (D), historical observations of C.E. 1707 tsunami run-up in Uwajima and Yoshoda (E and F, respectively) (Murakami et al., 1995), Ikata Power (G), and the Median Tectonic Line (dashed red line) (Tsutsumi and Okada, 1996). (Right) Maps of Lake Ryuuoo, Lake Amida, and Lake Kamega showing primary coring locations relative to lake bathymetry, along with locations of modern coastal structures and topography of the surrounding areas (modified from maps by the Geospatial Information Authority of Japan).

Table 1.1. Radiocarbon data. Lake Ryuuoo, Amida, and Kamega radiocarbon dates and calibrated ages (2 sigma range) in calendar years Before Present (yrs BP) using IntCal13 (Reimer et al., 2013), where C.E. 1950 is defined as "Present" by convention.

Index number	Lab number	Core	Depth (cm)	^{14}C age	Cal yrs BP (2σ)	Material dated
1	112518	RYU1	226	210 ± 20	0 - 301	Plant/wood
2	112519	RYU1	301.5	160 ± 20	0 - 283	Plant/wood
3	112520	RYU1	440 - 441	620 ± 20	553 - 656	Plant/wood
4	112521	RYU1	566 - 567	925 ± 20	792 - 912	Plant/wood
5	112522	RYU1	630	1005 ± 20	834 - 962	Plant/wood
6	112523	RYU1	922	2540 ± 20	2506 - 2745	Plant/wood
7	47636	AMI2	259	200 ± 30	0 – 303	Plant/wood
8	OS-89699	AMI2	294	565 ± 65	510 – 659	Aquatic plant
9	OS-89572	AMI2	384	1590 ± 35	1403 – 1553	Aquatic plant
10	OS-89518	AMI2	424 – 425	1780 ± 25	1618 – 1809	Plant/wood
11	OS-89335	AMI2	472 – 473	2210 ± 30	2148 – 2319	Plant/wood
12	OS-89336	AMI2	493 – 494	2460 ± 25	2379 – 2705	Plant/wood
13	OS-112351	KAM2	236	145 ± 30	2 – 282	Plant/wood
14	112513	KAM2	415	1100 ± 20	961 – 1057	Plant/wood
15	112514	KAM2	504	1575 ± 20	1411 – 1526	Plant/wood
16	112515	KAM2	527	1680 ± 20	1538 – 1685	Plant/wood
17	112516	KAM2	576	1955 ± 20	1833 – 1967	Plant/wood
18	112517	KAM2	689	3130 ± 20	3258 – 3396	Plant/wood

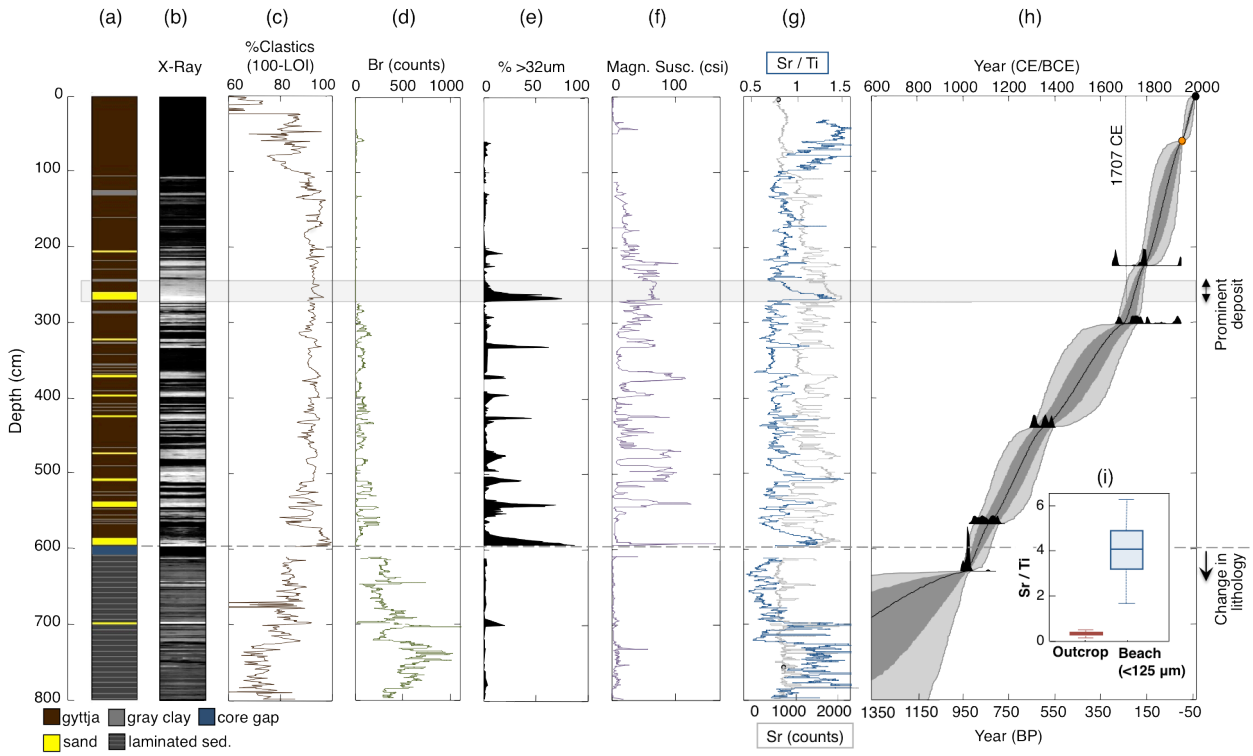

Figure 1.2. Depth profiles for core RYU1 (Lake Ryuuoo; see Fig. 1.1 for location)**.** (a) Stratigraphy column with key below. (b) X-radiograph, with light horizontal bands indicating dense, event deposition. (c) Percent clastic material (obtained from loss-on-ignition analysis). (d) Relative abundance of Br, expressed as XRF total counts integrated over the element's peak spectral area. (e) Coarseness, defined by the mass percent in excess of 32 µm. (f) Magnetic susceptibility. (g) Sr / Ti count ratio (blue) and Sr raw counts (gray). (h) Bayesian depth-to-age model constrained by the C.E. 1954 onset of ^{137}Cs (orange circle) and probability distributions for ^{14}C age controls (black filled curves). To provide more detail over the last millennia, the lowest ^{14}C age at 922 cm (index #6 in Tab. 1.1) extends beyond the age bounds in h. Black line in h denotes the median Bayesian-derived age, and 68% and 95% high density regions (HDRs) of the posterior age distributions (light and dark gray shaded regions, respectively) indicate the uncertainties of ages assigned to depths between age controls. (i) Interquartile ranges of Sr/Ti count ratios for discrete terrigenous (red) and barrier beach (blue) surface samples.

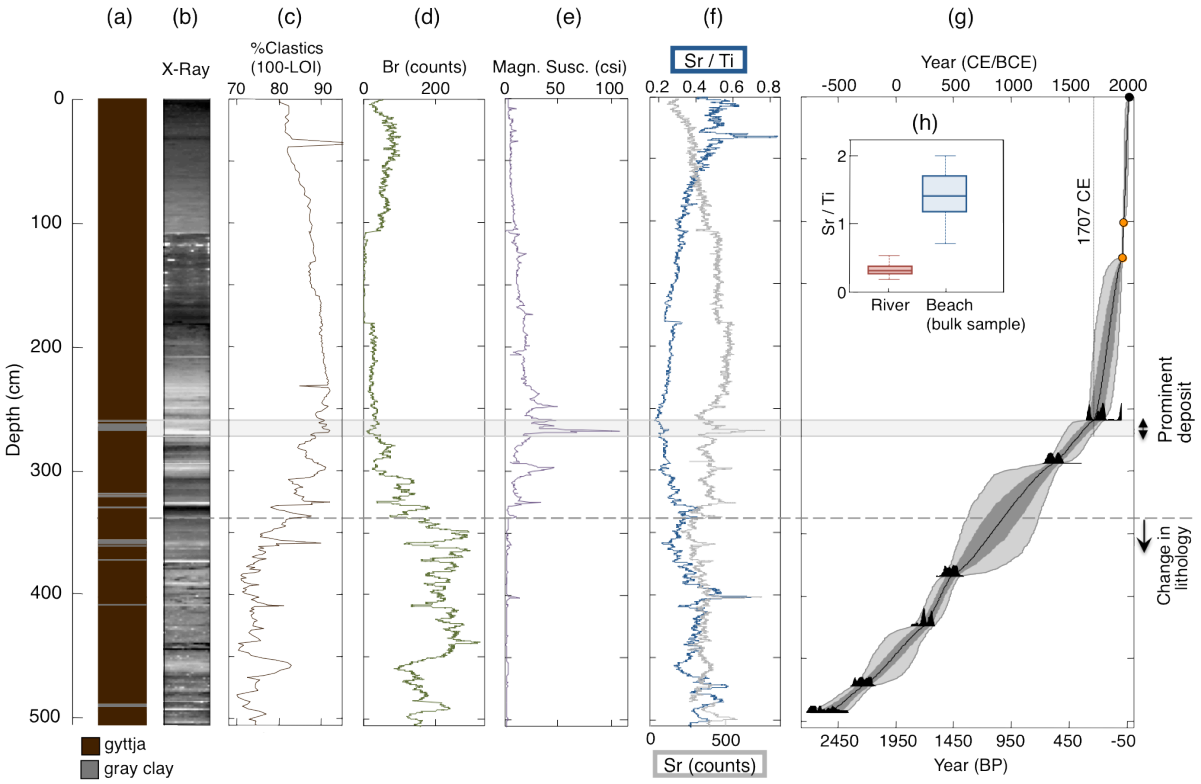

Figure 1.3. Depth profiles for core AMI2 (Lake Amida; see Fig. 1.1 for location)**.** (a) Stratigraphy column. (b) X-radiograph. (c) Percent clastic material. (d) Relative abundance of Br. (e) Magnetic susceptibility. (f) Sr / Ti count ratio (blue) and Sr raw counts (gray). (g) Bayesian depth-to-age model constrained by the C.E. 1954 onset and C.E. 1963 peak in ^{137}Cs (lower and upper orange circles, respectively) and probability distributions for ^{14}C age controls, following the same format as Fig. 1.2h. (h) Interquartile ranges of Sr/Ti count ratios for discrete fluvial (red) and barrier beach (blue) surface samples.

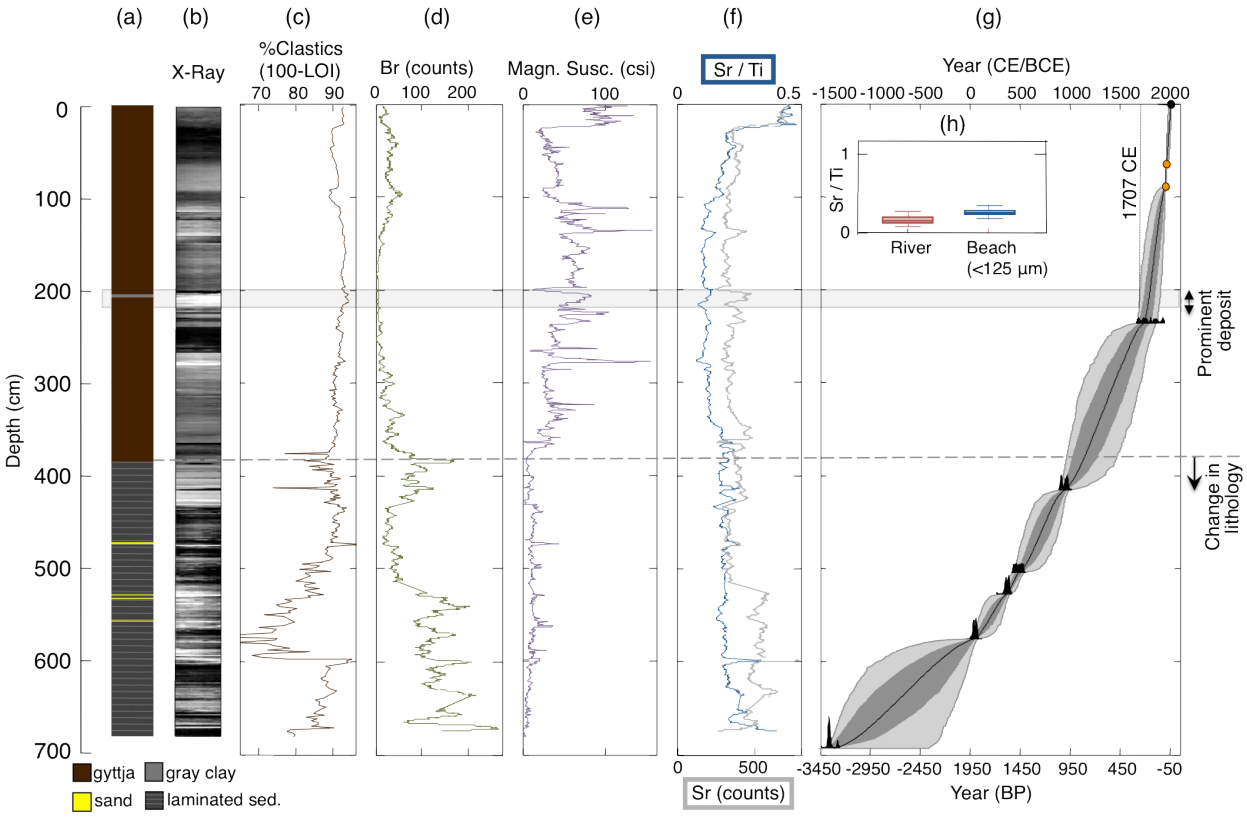

Figure 1.4. Depth profiles for core KAM2 (Lake Kamega, see Fig. 1.1 for location)**.** (a) Stratigraphy column. (b) X-radiograph. (c) Percent clastic material, (d) Relative abundance of Br. (e) Magnetic susceptibility. (f) Sr / Ti count ratio (blue) and Sr raw counts (gray). (g) Bayesian depth-to-age model, following the same format as Figs. 1.2h and 1.3g. (h) Interquartile ranges of Sr/Ti count ratios for discrete fluvial (red) and barrier beach (blue) surface samples.

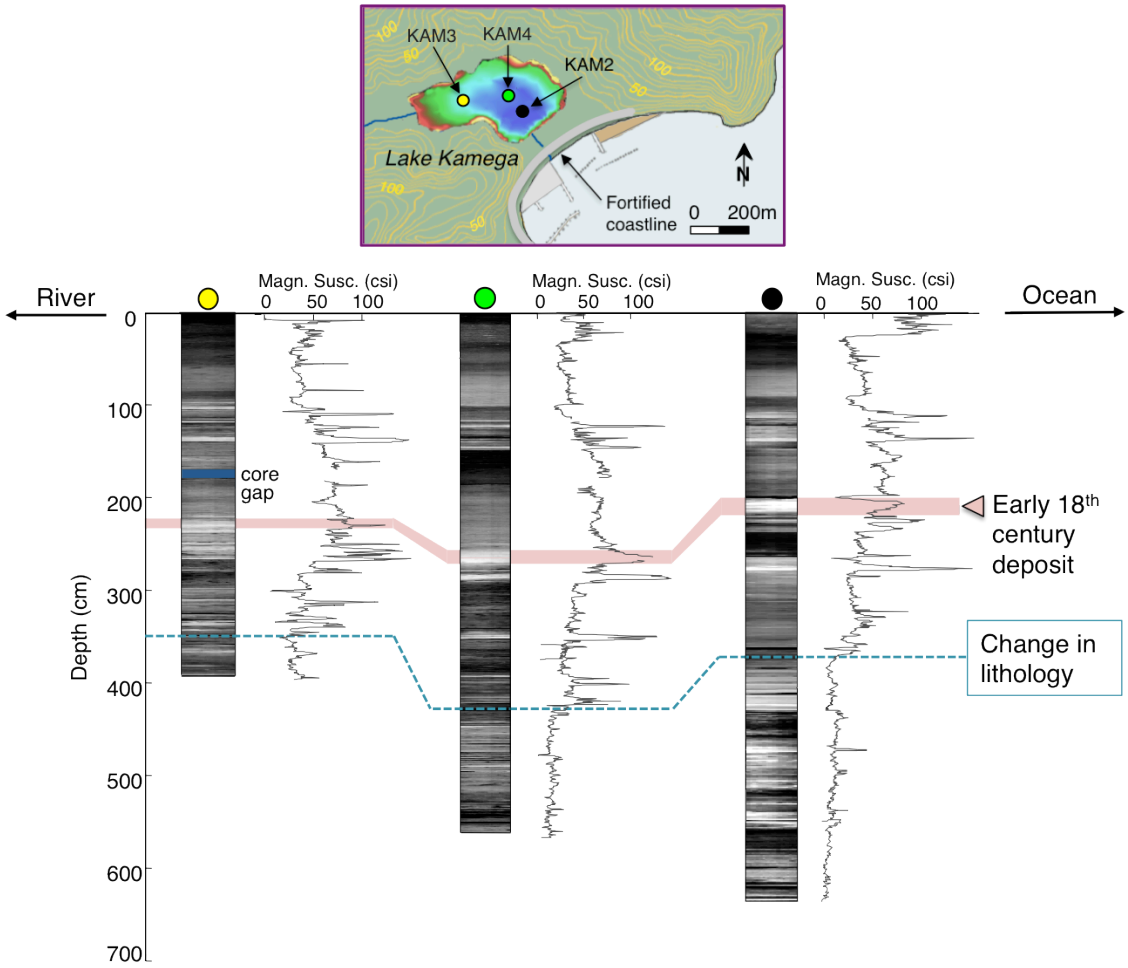

Figure 1.5. X-radiographs and magnetic susceptibility depth profiles for a transect of Lake Kamega cores (shown in top panel)**.** Deposit dating to the early 18th century in KAM2 (Fig. 1.4) is noted and traced through the transect (red shading), along with the older change in lithology (blue dashed line).

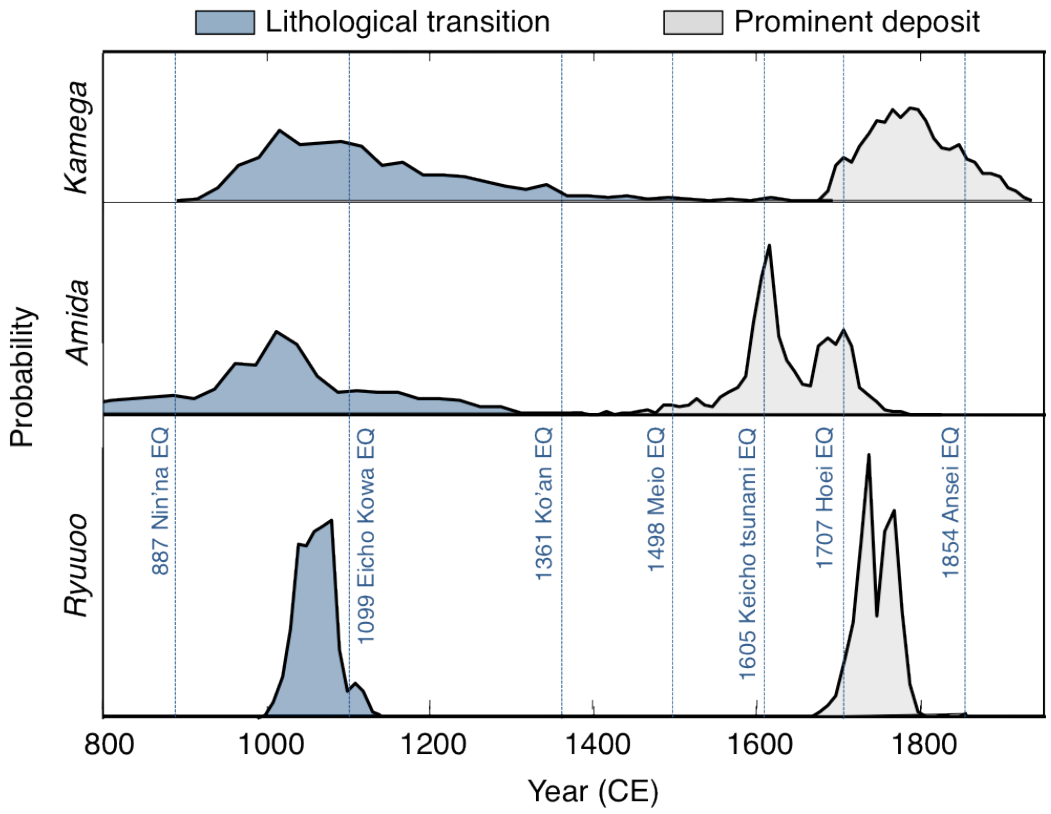

Figure 1.6. Bayesian-derived age probability distributions at the depths of the most prominent event deposit (gray) and of the lithological transition (blue) at each site. Blue dashed lines indicate the timing of historically documented Nankai Trough megathrust earthquakes (Ishibashi, 2002).

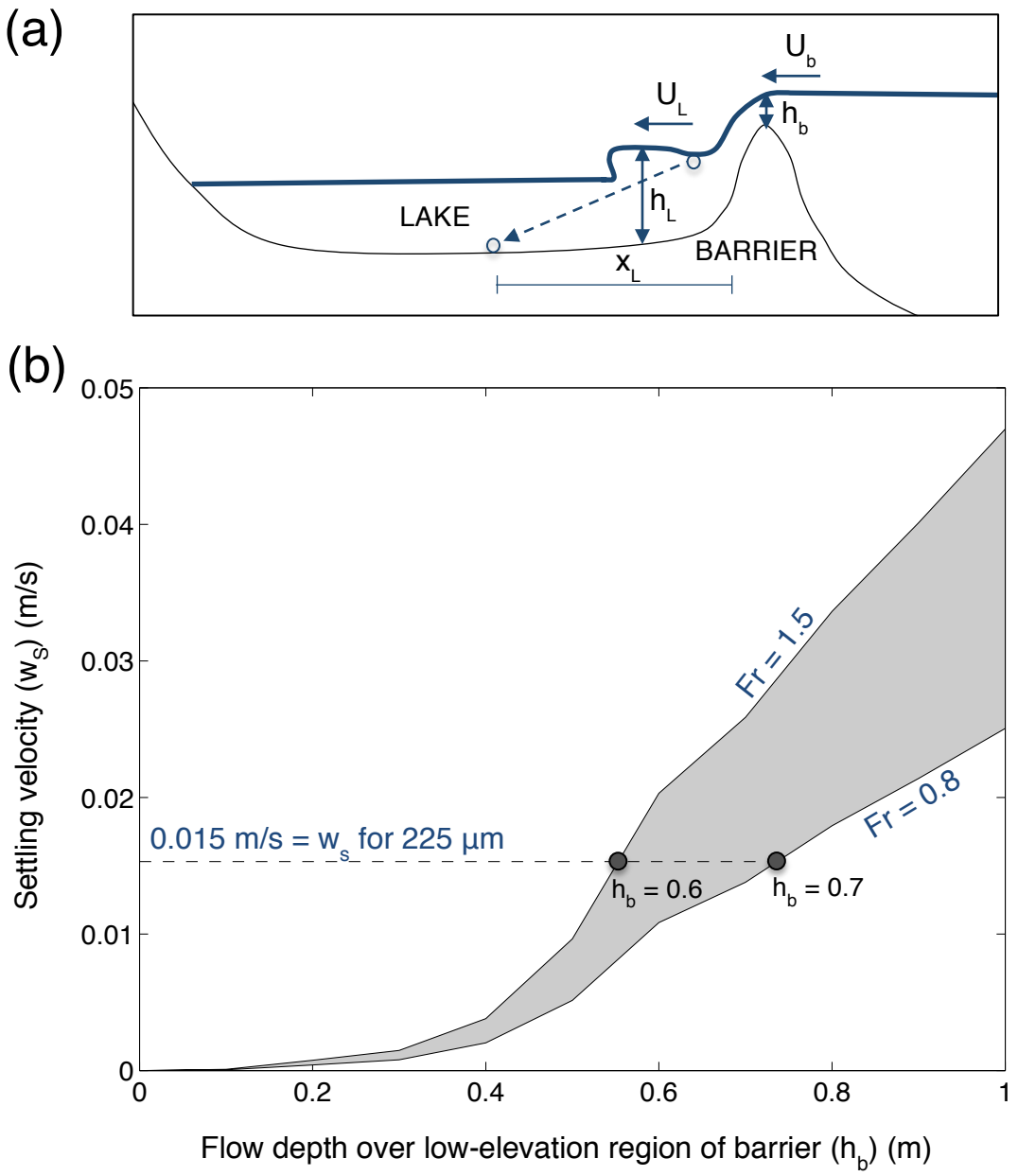

Figure 1.7. Woodruff et al. (2008) advective settling model variables and calculations. (a) Cross-section of tsunami inundation of a back-barrier lake illustrating Woodruff et al. (2008) advective settling model variables described in the text. The black and blue lines show land and water surfaces, respectively. (b) Relationship between tsunami flow depth over the lowest region of Lake Ryuuoo's barrier (h_b) and maximum settling velocity (w_S) for a grain transported from the low-elevation region of the barrier to the location of core RYU1, calculated from Eq. 7 for Froude numbers ranging from 0.8 to 1.5. h_b for a 225 µm grain (the D_{95} grain size observed in the 1707 deposit in RYU1) equals 0.6 – 0.7 m.

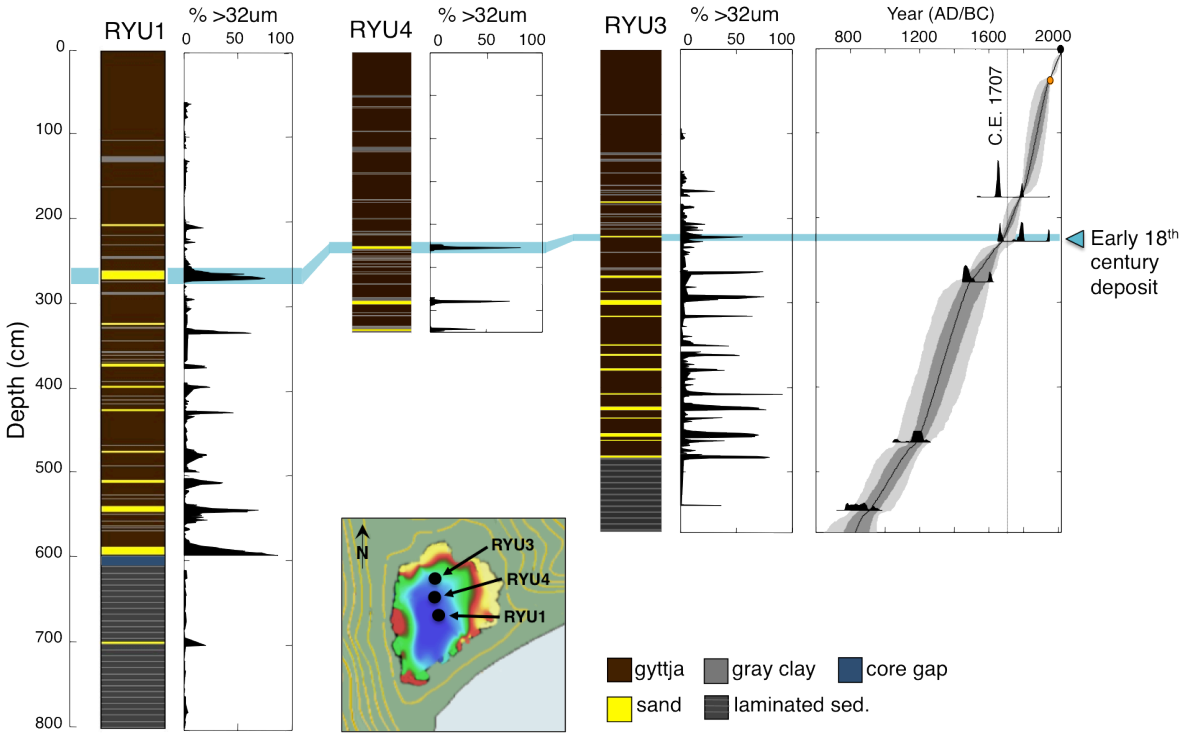

Figure 1.8. Stratigraphy columns (key below) **and percent coarse depth profiles for the transect of Lake Ryuuoo cores** (locations shown in lower map)**.** Deposit dating to the early 18th C in RYU1 is noted and traced through the transect (blue shading). The deposit was identified in RYU4 by matching the core's stratigraphy to RYU1. It was identified in RYU3 using the Bayesian depth-to-age model plotted on the right (age model follows the same format as Figs 1.2h, 1.3g, and 1.4g).

CHAPTER 2

SIMULATING TSUNAMI INUNDATION OF LAKE RYUUOO IN SHIKOKU, JAPAN TO TEST NEW AND EXISTING SOURCE MODELS FOR THE C.E. 1707 HŌEI EARTHQUAKE

2.1 Abstract

Much of our current knowledge of the C.E. 1707 Hōei earthquake comes from historically recorded observations of the resultant tsunami. Thus, pairing earthquake models with tsunami inundation simulations that can be compared to these observations is a valuable tool for exploring the validity of various rupture scenarios. Existing source models for the Hōei earthquake have failed to match historical records of a 5 m tsunami impacting the northeastern Bungo Channel without also overestimating tsunami heights along the open Pacific coasts of western Shikoku and eastern Kyushu (Furumura et al., 2011; Hyodo et al., 2014); however, historians have pointed to significant uncertainties related to the reliability of these historical tsunami records (Ishibashi, 2004; Ando, 1975; Murakami et al., 1995). In Chapter 1, we presented the first geologic evidence of the Hōei tsunami from the northern Bungo Channel, where a marine flood deposit preserved in back-barrier Lake Ryuuoo provided a height estimate of 3 – 4 m for the 1707 tsunami. Given this new and independent constraint, we re-examine the validity of the Hōei earthquake source models by Furumura et al. (2011) and Hyodo and Hori (2013) by testing their ability to overtop Lake Ryuuoo's barrier beach. We then test a series of new earthquake scenarios by making the assumption that coseismic slip follows present-day patterns of geodetically imaged interseismic coupling.

We use GeoClaw, an open source tsunami model, to simulate tsunami runup generated from various earthquake scenarios on a high-resolution bathymetric grid around Lake Ryuuoo. Both the Furumura et al. (2011) and Hyodo and Hori (2013) earthquake sources are unable to produce a model tsunami that inundates Lake Ryuuoo and are therefore inconsistent with sedimentological evidence of the Hōei tsunami preserved in the lake. The coupling-based earthquake scenarios, however, generate a tsunami that is more consistent with both historical and sedimentological observations in southwestern Japan. They produce less coseismic uplift offshore and greater subsidence inland, generating a smaller tsunami on the open Pacific coastline of Shikoku and a larger tsunami in the northern Bungo Channel that is able to inundate Lake Ryuuoo with sufficient flow for producing the deposit we observe. These finding suggest that spatial trends in present-day coupling models may be consistent with past periods of coseismic rupture along the Nankai Trough.

2.2 Introduction

Numerical simulations of tsunami inundation are a powerful tool for evaluating earthquake scenarios and assessing tsunami hazard (e.g. Tang et al., 2009; Fritz et al., 2011; Furumura et al., 2011; Hyodo et al., 2014). This is especially true for southwestern Japan, where the largest known Nankai Trough earthquake occurred in C.E. 1707, predating the instrumental record (e.g. Ishibashi, 2004). Much of our current knowledge of the C.E. 1707 Hōei earthquake comes from historical observations of the resultant tsunami; thus, these documented tsunami run-up heights are a key metric for validating models of high-magnitude Nankai Trough earthquake scenarios.

2.2.1 Existing models for the C.E. 1707 Hōei earthquake

Recently, Furumura et al. (2011) and Hyodo et al. (2014) have run tsunami simulations for Hōei earthquake source models to compare the maximum model-derived tsunami heights to historical observations. Furumura et al. (2011) (F11) first tested the kinematic source model published by An'naka et al. (2003), which defined relative slip for the event on four rectangular fault planes. They found that simulated tsunami heights matched historical observations along Japan's Pacific coast from Tosa Bay to Suruga Bay (locations shown in Fig. 2.2a), but farther to the southwest along the coasts of western Shikoku and eastern Kyushu, simulated heights were less than half of observed heights.

Following the discovery of a sequence of prominent marine sand deposits on the eastern coast of Kyushu in Lake Ryujin (Fig. 1.1) that were consistent with the timing of documented C.E. 1707, C.E. 1361, and C.E. 684 Nankai Trough earthquakes (Okamura et al., 2004), F11 revised the An'naka et al. (2003) source model by adding a fifth subfault segment that extended the rupture area for the C.E. 1707 earthquake an additional 80 km to the southwest (segment N5' in Fig. 2.2 and Tab. 2.1). Resulting tsunami heights increased along the Pacific coast of western Shikoku and eastern Kyushu, better matching historical observations, and modeled flow speeds around Lake Ryujin were sufficient for transporting grain sizes observed in the lake's tsunami deposits. However, this revised model only produced a 2 – 3.5 m tsunami farther inland within the Bungo Channel, where historical observations from the northwestern Shikoku villages of Uwajima and Yoshoda (Fig. 1.1) described a 5-m tsunami (Murakami et al., 1995).

The subfault format of the F11 model is highly simplified, both because it does not capture the complex geometry of the Nankai plate interface, and because it does not allow for

variation in slip in the direction perpendicular to the strike of the plate interface. Variation in coseismic slip in this strike-perpendicular direction can have a large effect on the resultant tsunami, as was demonstrated by the 2011 Tōhoku event. In part, the 2011 tsunami was unexpectedly high because large coseismic slip occurred within the shallow, up-dip region of the plate boundary near the axis of the Japan Trench (e.g. Fujiwara et al., 2011). Recent drilling studies have also found that shallow slip may have occurred along the Nankai Trough during past earthquakes (Sakaguchi et al., 2011) and have motivated the development of new large Nankai earthquake scenarios that account for the possibility of shallow slip. Hyodo and Hori (2013) (HH13) produced one of these scenarios by using realistic boundary conditions for plate geometry and convergence rate and imposing heterogeneous fracture energy in the shallow regions of the plate interface to simulate the earthquake generation cycle of the trough. They successfully reproduced the observed pattern of alternately occurring smaller magnitude earthquakes with a recurrence interval of ~100 – 200 yrs, such as the C.E. 1854 and C.E. 1946 earthquakes, and larger magnitude earthquakes with a recurrence interval of ~300 – 400 yrs, such as the C.E. 1707 earthquake. In the larger scenario, the rupture area extended as far to the southwest as the F11 model did, but large coseismic slip extending up-tip to the trench axis resulted in a moment magnitude ($M_W \sim 9$) that was larger than previously estimated.

Subsequently, Hyodo et al. (2014) ran tsunami simulations based on the large earthquake scenario by HH13, but they struggled to match historical observations of C.E. 1707 tsunami height in the same regions as the F11 simulations did. The domain of their simulations extended farther north into the Seto Inland Sea (Fig. 1.1), and they found that while the HH13 earthquake scenario was able to produce a 5 m tsunami within the Bungo

Channel near Uwajima and Yoshoda, it generally overestimated tsunami heights along the Pacific coasts of Shikoku and Kyushu. They also experimented with three additional scenarios where they limited slip in the large earthquake model to the seismogenic zone, to the seismogenic zone plus an up-dip extension, and to the seismogenic zone plus a down-dip extension. However, they found that the scenario that provided the best match to historical observations along the Pacific coastlines of Shikoku and Kyushu also underestimated tsunami heights within the northern Bungo Channel and Seto Inland Sea.

2.2.2 Modern observations of interplate coupling along the Nankai Trough

HH13 took a simulation-based approach to modeling the behavior of the Nankai plate boundary; however, over the last couple decades, geodetic measurements from Global Positioning System (GPS) networks have provided unprecedented insight into the current behavior of subduction zones around the world. During interseismic periods, the seismogenic zone of a subduction interface remains locked by friction, and the crust accumulates a slip deficit. GPS measurements that track spatial and temporal variation in crustal motion can be used to estimate this slip deficit and form models of interseismic coupling (e.g. Loveless and Meade, 2010; Bürgmann et al., 2005). Coupling is a measure of the degree to which two plates are locked together during interseismic stress buildup and is defined as slip deficit, normalized by the relative motion between the overriding and subducting plates. Recent studies have reported a positive correlation between the spatial signature of interseismic coupling and of subsequent coseismic slip, based on both numerical simulations (Kaneko et al., 2010), and observations of modern events such as the 2011 Tōhoku earthquake (e.g. Loveless and Meade, 2011).

Many models of interseismic coupling have been developed along the Nankai Trough (e.g. Savage and Thatcher, 1992; Le Pichon et al., 1998; Mazzotti et al., 2000; Miyazaki and Heki, 2001; Heki and Miyazaki, 2001; Ito and Hashimoto, 2004; El-Fiky and Kato, 2006; Tabei et al., 2007; Hashimoto et al., 2009; Liu et al., 2010; Loveless and Meade, 2010). While many exclusively focus on subduction zone coupling, the model by Loveless and Meade (2010) uses spherical linear block theory (Meade and Loveless, 2009) to simultaneously estimate the long-term motion of crustal blocks, slip rates on block-bounding faults, and the spatially varying fault slip rates on subduction zone interfaces; thus, their model is unique in that it includes the effects of onshore crustal faults when fitting the GPS data. Hok et al., (2011) published several dynamic rupture scenarios for the Nankai Trough based on coupling estimates by Hashimoto et al. (2009); however, no tsunami simulations have been run to validate their coupling-based scenarios.

2.2.3 Sedimentological records of the Hōei event from the Bungo Channel

Historical observations from the C.E. Hōei 1707 tsunami currently provide the best means for validating large rupture scenarios for the Nankai Trough; however, historians have pointed to significant uncertainties related to the reliability of these records (Ishibashi, 2004; Ando, 1975; Murakami et al., 1995). Sedimentological reconstructions of tsunami inundation from Lake Ryuuoo, Lake Amida, and Lake Kamega presented in Chapter 1 provide the first means to independently assess flooding from the Hōei tsunami within the Bungo Channel. A marine overwash deposit consistent with the timing of the C.E. 1707 Hōei event was preserved in all three lakes, and the deposit's grain size at Lake Ryuuoo, the most pristine of the three sites, provided a height constraint of 3 – 4 m for the Hōei tsunami.

Here, we run high-resolution tsunami simulations around Jio Island in order to assess whether this new C.E. 1707 tsunami height constraint from Lake Ryuuoo is consistent with the smaller flooding elevations produced by the F11 and HH13-based simulations or with the higher, historically documented flooding elevations from Uwajima and Yoshoda. More specifically, we simulate tsunami runup around Lake Ryuuoo on a high-resolution bathymetric grid to test whether existing earthquake models generate a tsunami that overtops the lake's barrier with a sufficient flow to create the observed tsunami deposit. We then test two new, observation-based earthquake scenarios by making the large assumption that the spatial distribution of coseismic slip follows patterns of modern-day interseismic coupling estimated by Loveless and Meade (2010).

2.3 Tsunami simulations of the C.E. 1707 Hōei event

2.3.1 The GeoClaw Numerical Model

Numerical modeling of tsunami inundation was performed using version 5.3.0 of the open source tsunami model GeoClaw (GeoClaw et al., 2015). GeoClaw models flow over varying topography using high-resolution finite volume methods to solve the nonlinear shallow water equations and has undergone extensive validation testing using real events and synthetic test problems (LeVeque and George, 2007; Berger et al., 2011; González et al., 2011; LeVeque et al., 2011). The shallow water equations are a two-dimension, depth-averaged system of partial differential equations:

$$h_t + (hu)_x + (hv)_y = 0,$$

$$(hu)_t + (hu^2 + \frac{1}{2}gh^2)_x + (huv)_y = -ghB_x - Dhu,$$

$$(hv)_t + (huv)_x + (hv^2 + \tfrac{1}{2}gh^2)_y = -ghB_y - Dhv,$$

(1)

where *u(x,y,t)* and *v(x,y,t)* are the depth-averaged eastward and northward velocities, respectively, *h(x,y,t)* is fluid depth, *B(x,y)* is bathymetry, and subscripts denote partial derivatives. *D(h,u,v)* is a drag coefficient given by:

$$D(h,u,v) = n^2 g h^{-4/3} \sqrt{u^2 + v^2} \quad (2)$$

where *n* is the Manning coefficient, determined by the seafloor or land surface roughness. This is the only adjustable parameter in the GeoClaw model, and for tsunami modeling, a constant value of $n = 0.025$ $m^{-1/3}$ s is commonly used for the seafloor (e.g. Arcos and LeVeque, 2015).

2.3.2 Topographic model

Seven different topography and bathymetry datasets were merged to create four uniformly spaced, rectangular topography grids with increasingly finer resolution around Lake Ryuuoo. The 1-arc minute resolution ETOPO1 global topography and bathymetry model (Amante and Eakins, 2009) was used over the entire computational domain, from 129° E to 141° E and from 30° N to 37° N (Fig. 2.1a). Around Kyushu and Shikoku, the J-EGG500 500 m resolution bathymetric grid, published by the Japan Oceanographic Data Center, was merged with the Global 30 Arc-Second Elevation (GTOPO30) dataset, available from the U.S. Geological Survey, to create a 0.005° (~500 m) resolution grid (Fig. 2.1b). In the northeastern Bungo Channel, a paper nautical chart (Japan Coast Guard, 2001) was digitized and merged with the Advanced Spaceborne Thermal Emission and Reflection Radiometer (ASTER) Global Digital Elevation Model (GDEM) to create a 0.002° (~200 m) resolution grid (Fig. 2.1c), and around Jio Island, bathymetric data from a survey performed

by Arc Geo Support Co., Ltd using a C3D sidescan sonar system on July 21, 2014 was merged with a 5 m resolution DEM of Jio Island, published by the Geospatial Information Authority of Japan, to create a 0.00005° (~5 m) resolution grid around Lake Ryuuoo (Fig. 2.1d). All topography and bathymetry data was adjusted in reference to MSL.

2.3.3 Tsunami sources

2.3.3.1 F11 model

An analytical solution for vertical topography displacement resulting from the F11 subfault model (Fig. 2.2a) can easily be calculated by applying the Okada model (Okada, 1985) to each of the five subfault segments and summing the displacements calculated for each. Tab. 2.1 lists the parameters that define the five F11 subfault segments, and vertical topography displacement was calculated from these parameters using the GeoClaw *dtopotools* module.

2.3.3.2 HH13 model

Dr. Jack Loveless, assistant professor of geosciences at Smith College, performed all calculations described here and in Chapter 2.3.3.3 for converting coseismic slip distributions to vertical topography displacement. First, a seismically imaged geometry of the Nankai plate interface by Hirose et al. (2008) was triangulated into discrete dislocation elements, and partial derivatives relating unit strike and unit dip to horizontal and vertical displacement were calculated for each dislocation element. Slip magnitudes from the large earthquake scenario in Hyodo and Hori (2013) were digitized (Fig. 2.3a) and projected onto the Hirose et al. (2008) fault geometry (Fig. 2.3b), and the rake of slip was assumed to equal the long-term

direction of plate convergence along the Nankai Trough (hereafter referred to as long-term plate motion) estimated by Loveless and Meade (2010). Slip rake was then also projected onto the fault geometry and multiplied by slip magnitude to determine strike-slip and dip-slip for each dislocation element. Finally, the dip-slip values were multiplied by the partial derivatives to calculate vertical coseismic surface deformation for the HH13 scenario (Fig. 2.3c).

2.3.3.3 Coupling-based models

Two additional sets of rupture scenarios were generated by making the large assumption that the spatial distribution of coseismic slip follows patterns of modern-day interseismic coupling estimated by Loveless and Meade (2010) (Fig. 2.4a). For these two sets of coupling-based scenarios, hereafter referred to as the long-term plate motion (LTM) and the slip deficit (SD) scenarios, coupling was scaled to coseismic slip using two different methods: for LTM scenarios, slip deficit values were normalized by long-term plate motion, and the rake of slip was assumed to equal the direction of long-term plate motion. For the SD scenarios, slip deficit values were normalized by the maximum slip deficit along the plate interface, and rake of coseismic slip was assumed to equal the rake of estimated slip deficit. In both cases, slip magnitudes were scaled to produce rupture scenarios with moment magnitudes ranging from ~M_W 8.95 – 9.1, following magnitude estimates from Hyodo and Hori (2013) and an official government risk-assessment report (Cabinet Office, 2012). Fig. 2.4b shows relative slip magnitudes projected onto the fault interface, and slip magnitude and direction were used to calculate vertical surface deformation patterns for the coupling-based LTM (Fig. 2.4c) and SD (Fig. 2.4d) scenarios following the methods described in 2.3.2.2.

2.3.4 GeoClaw parameters

In all GeoClaw simulations, tsunamis were generated by instantaneously displacing the ocean floor following one of the distributions of vertical coseismic surface deformation described in 2.3.3 and illustrated in Figs 2.2b, 2.3c, 2.4c, and 2.4d. As the tsunami was propagated across the ocean, GeoClaw used a block-structured adaptive mesh refinement (AMR) algorithm that increased grid resolution and decreased the time step around the tsunami and in pre-defined regions of interest (George, 2006, 2008; George and LeVeque, 2006; Leveque et al., 2011). At the coarsest level, a 0.5° (~50 km) grid resolution was used. Three additional nested levels of refinement, down to ~500 m resolution, tracked the tsunami into the northeastern Bungo Channel, where two more refinement levels of ~250 m and ~5 m were used to resolve tsunami inundation of Lake Ryuuoo (Fig. 2.1). While spatial refinement ratios were user-specified, GeoClaw automatically chose temporal refinement ratios to achieve a desired Courant number:

$$C = \frac{u\Delta t}{\Delta x} \tag{3}$$

where C is the Courant number, u is flow velocity magnitude, Δt is the time step, and Δx is the grid cell length. The desired C value was set to 0.75 in our simulations. Initial low-resolution model runs revealed that the first wave consistently produced the largest runup within the Bungo Channel 1 - 2 hours after model initialization, so subsequent high-resolution simulations were run for 3 hours.

Following the setup of F11, Manning's roughness coefficients were set to 0.025 $m^{-1/3}$ s and 0.04 $m^{-1/3}$ s in the ocean and on land, respectively. Model gauges that monitored water depth, water surface elevation, and momentum in the x (east) and y (north) directions at

every time step were placed around Jio Island, and GeoClaw's fixed grid monitoring tool was used to output maximum water surface elevations along the Pacific coastlines of Kyushu and Shikoku. Tsunami heights were not monitored along the Seto Inland Sea coastline due to difficulty in finding sufficiently high-resolution bathymetric data to resolve its complex bathymetry.

2.3.5 Validation of GeoClaw simulations

In order to validate the GeoClaw model setup, GeoClaw calculations of maximum tsunami height for the F11 earthquake source were compared to the model-derived tsunami heights originally published in Furumura et al. (2011) and calculated using a nonlinear long-wave tsunami model by Goto and Ogawa (1997). Fig. 2.5 compares the maximum tsunami height calculations from the two models along Kyushu and Shikoku's Pacific coasts to historical observations of the C.E. 1707 tsunami. There was good agreement among the general trends in tsunami height from all three sources, and differences in the details of the two model calculations were likely due to the differing spatial resolutions of the models and to the difficulty in precisely matching the along-coastline distances (i.e. aligning the x-axes).

The original F11 simulation was run on a 90 m or 30 m mesh in nearshore regions, while the GeoClaw simulation was run on a ~500 m mesh along most of southwestern Japan's coast (AMR level 4; Fig. 2.1b) due to limitations in publicly accessible bathymetry data. Tsunami models are highly sensitive to grid resolution in the nearshore, and a 500 m mesh is generally not sufficient for resolving coastal tsunami inundation in detail (e.g. Tang et al., 2009). However, Fig. 2.5 shows that a 500 m mesh reproduced the same range in tsunami heights within the Bungo Channel and is therefore sufficient for propagating the

tsunami up to the two additional higher resolution levels of mesh refinement that surround Lake Ryuuoo (Figs. 2.1c and 2.1d).

2.4 Model results

2.4.1 F11 results

GeoClaw simulations of the F11 Hōei earthquake scenario yielded the same inconsistency between historical observations and model-derived tsunami heights in the northern Bungo Channel near Uwajima as was reported in Furumura et al. (2011) (Fig. 2.5). The high-resolution simulation around Jio Island also revealed that the F11 tsunami failed to inundate Lake Ryuuoo. Fig. 2.7 shows results from two model tide gauges at Lake Ryuuoo, where gauge 1 was located 40 m seaward of the barrier and was initially at MSL, and gauge 2 was located on the lowest-elevation region of the barrier and was initially 3.1 m above MSL. The gauges recorded 40 cm of coseismic ground subsidence, and maximum tsunami height reached ~2 m (Fig. 2.7b), where tsunami height is defined as the distance between post-subsidence sea level and the tsunami wave crest. The 2 m tsunami was too small to overtop the barrier, so gauge 2 recorded no flow (Fig. 2.7c).

In order to explore the limitations of the subfault model, we also ran a series of simulations where we incrementally increased the amount of slip on the N5' fault segment (Fig. 2.2) until Lake Ryuuoo was inundated. Barely overtopping the lowest region of the barrier required increasing slip along N5' by a factor of 2.4, from 9.2 m to 22.08 m.

2.4.2 HH13 results

The HH13 model yielded the same inconsistencies with historical observations as the F11 model did. Model-derived tsunami heights were lower than observed heights in the northern Bungo Channel near Uwajima, and they either matched or were larger than observed heights along the Kyushu coast and along the Shikoku coast from Tosahimizu to Cape Muroto (Fig. 2.6). Compared to the tsunami simulation of the same HH13 source model run by Hyodo et al. (2014), our simulation produced a tsunami that was 1 – 2 m shorter everywhere along southwestern Japan's coast. This was likely because we used a more corrugated fault geometry for the Nankai interface that translated more of the total slip into strike-sip, and because the rake we assigned to coseismic slip (matching long-term plate motion) was likely different.

Model tide gauges around Jio Island recorded 80 cm of coseismic subsidence and a ~2.5 m high tsunami (Fig. 2.7b) that produced 10 cm of flow over the narrow, low-elevation region of the barrier (Fig. 2.7d). An additional model tide gauge placed on the water surface of Lake Ryuuoo showed that the 10 cm flow spread and shallowed to a 1 cm-deep flow behind the barrier.

2.4.3 Coupling model results

Compared with the HH13 model, coseismic slip in the coupling-based scenarios was focused farther inland to a region underlying Shikoku (Fig. 2.4b), where GPS data indicate the strongest coupling (Loveless and Meade, 2010). GPS data also show that the Nankai interface is weakly coupled near the trench axis, so there was less shallow slip in the coupling-based models than in the HH13 model. The resulting vertical surface deformation

was sensitive to the chosen rake of slip, as the deformation patterns significantly differed for the coupling-based LTM and SD scenarios (Figs 2.4c and 2.4d, respectively).

Fig. 2.6 compares maximum tsunami heights for the two sets of coupling-based scenarios to heights from the HH13 model and from historical observations. The coupling-based models generally raised tsunami heights everywhere along Kyushu's coast and along the northwestern coast of Shikoku from Sata to Sukomo, and they lowered tsunami heights on the open Pacific coast of Shikoku from Tosahimizu to Cape Muroto. The higher-magnitude coupling models (nearer to M_W 9.1) also generally provided a better match to historical observations than the lower-magnitude models (~M_W 8.95) did.

Model tide gauges showed that all of the coupling-based scenarios inundated Lake Ryuuoo. The LTM scenarios caused ~1.5 – 2 m of subsidence around Jio Island and a 3 – 5 m high tsunami (Fig. 2.7b), with flow depths of 0.5 – 2.5 m over the low-elevation region of the barrier (Fig. 2.7e). The SD earthquake scenarios of similar moment magnitudes inundated Lake Ryuuoo more severely, as they caused Jio Island to subside ~1.5 – 2.5 m and generated a 4 – 7 m high tsunami (Fig. 2.7b), with flow depths of 1.5 – 4 m over the low-elevation region of the barrier (Fig. 2.7f).

2.5 Discussion

2.5.1 Evaluation of source models

High-resolution GeoClaw tsunami simulations around Jio Island revealed that the F11 and HH13 Hōei earthquake source models were unable to produce tsunamis consistent with the C.E. 1707 tsunami deposit preserved in Lake Ryuuoo. The F11 tsunami simulation completely failed to overtop the barrier, and the HH13 simulation only overtopped the barrier

enough to produce a 1 cm-deep flow on the lake surface, which is insufficient for creating the 25 cm-thick deposit we observe (Fig. 1.2). These results support the notion that published source models are failing to capture some characteristic of the southwestern extent of Nankai subduction zone that would cause its rupture to produce a higher inland tsunami.

In the case of the F11 model, simply increasing the amount of average slip on the N5' fault segment did not inundate Lake Ryuuoo until slip reached an unrealistically high value of 22.08 m. This is unsurprising, given that the subfault format of the F11 model neither allows for slip variation in the strike-perpendicular direction, nor captures the complex geometry of the plate interface. The HH13 model accounts for both of these complexities, so its inconsistency with historical observations in the northern Bungo Channel and the 1707 deposit in Lake Ryuuoo indicates that extending the region of coseismic slip up-dip to the trench axis also does not sufficiently increase inland tsunami heights.

Although the coupling-based earthquake models do not clearly provide a better overall match to historical observations, they do raise tsunami heights in the northern Bungo Channel where the HH13 and F11 models were underpredicting them, and they lower tsunami heights on the open Pacific Shikoku coast where the HH13 model was overpredicting in places. Thus, this modeling approach shows promise for evening model-observation tsunami height discrepancies in southwestern Japan, and it suggests that spatial trends in present-day coupling may be consistent with past periods of coseismic rupture along the Nankai Trough. It is also important to note that the SD and LTM coupling scenarios produce visibly different inundation patterns, indicating that the rake of coseismic slip is a significant consideration in tsunami hazard modeling. The SD approach is more internally consistent, as it assumes that the rake of coupling is directly opposed by the

earthquake that releases the coupling; however, assuming that slip occurs in the direction of subduction, as we did in the LTM approach, may be more consistent with long-term rupture patterns. Thus, both approaches are justifiable and warrant consideration.

The coupling-based earthquake scenarios are also the only ones capable of inundating Lake Ryuuoo. Interestingly, although the higher magnitude coupling-based scenarios (~M_W 9.1) generally match historical observations best, they produce flow depths over Lake Ryuuoo's barrier that far exceed the 55 – 75 cm barrier flow depth estimate from the Woodruff et al. (2008) advective settling calculation presented in chapter 1.6.3. The lower magnitude earthquake scenarios (~M_W 8.95), which underpredict most of the historical observations, produce 0.5 – 1 m flows over the barrier that are more consistent with the advective settling constraint. While the advective settling model is suitable for roughly constraining flow depths, it is an inverse calculation that relies on many assumptions (see chapter 1.6.3); therefore, plans for future work include using high-resolution GeoClaw output of tsunami inundation in Lake Ryuuoo to run forward sediment transport models that produce a deposit we can compare to field observations. We are currently working with Virginia Tech professor Dr. Robert Weiss and PhD candidate Wei Cheng to develop these sediment transport calculations based on the model published in Cheng and Weiss (2013).

2.5.2 Model uncertainties

2.5.2.1 Tides

Tidal effects introduce uncertainty associated with constraining the minimum tsunami height required to inundate Lake Ryuuoo during the time of the C.E. 1707 event. Modern tide gauge records made available by the Japan Meteorological Agency demonstrate a time

lag in the tidal cycle between Japan's open Pacific coast and the northern Bungo Channel coast. This time lag leads to differences of several meters in water elevation at the two locations, which may affect the flow velocity or height of a tsunami propagating through the channel. Miyamoto et al. (2006) modeled this tsunami-tide interaction in the Bungo Channel and Seto Inland Sea but found that tides only increased tsunami height by a maximum of 0.5 m; however, Hyodo et al. (2014) was critical of the Miyamoto et al. (2006) model because it was run on a 450 m grid, which generally cannot accurately resolve nearshore tsunami heights (e.g. Tang et al., 2009).

2.5.2.2 Barrier stability

Our simulations around Lake Ryuuoo also rely on the assumption that the lake's barrier beach was near its current elevation of 3.1 – 3.8 m above MSL in C.E. 1707. Given the barrier's stable configuration between two protruding headlands in a region with low rates of sea-level rise and limited anthropogenic modifications, we believe that relatively consistent barrier height over the last 300 years is a reasonable assumption. The upper 2 m of Lake Ryuuoo's sedimentary record was likely deposited since C.E. 1820 (Fig. 1.2h) and does not contain coarse-grained overwash deposits (Fig. 1.2e). This absence might suggest a decrease in barrier sensitivity to overwash over this most recent interval. However, there is roughly a 200-yr return period for recorded overwash in the lower section core RYU1; i.e. the four coarsest-grained event deposits (excluding the deposit directly overlying the lithological transition) at sediment depths of 540 cm, 425 cm, 330 cm, and 270 cm (Fig. 1.2e) occur ~200 yrs, ~100 yrs, and ~240 yrs apart, respectively (Fig. 1.2h). Thus, the absence of a large overwash deposit between the C.E. 1707 event and C.E. 1900, which marks the onset of

anthropogenic fortifications to the barrier (see chapter 1.6.2), does not necessarily suggest a change in the barrier's sensitivity to overwash.

2.6 Conclusions

Based on the first geologic evidence of the Hōei tsunami from the northern Bungo Channel, we re-examine the validity of the earthquake source models by Furumura et al. (2011) and Hyodo and Hori (2013) by testing their ability to overtop Lake Ryuuoo's 3.1 – 3.8 m high barrier beach. Generating a tsunami from the Furumura et al. (2011) source that inundates Lake Ryuuoo requires increasing slip along the Nankai Trough's southwesternmost segment by an unrealistic factor of 2.4, from 9.2 m to 22.08 m and therefore points to limitations in kinematic earthquake source models for capturing the behavior of the southwestern extent of the Hōei earthquake rupture area. The tsunami from the Hyodo and Hori (2013) source only generates 1 cm of flow in Lake Ryuuoo, indicating that extending the region of coseismic slip up-dip to the trench axis also does not account for Hōei tsunami inundation patterns in the southwest.

We then test a series of new earthquake scenarios by making the assumption that coseismic slip follows present-day patterns of geodetically imaged interseismic coupling. Along the southwestern extent of the plate interface, there is a region of weak coupling up-dip along the trench axis and a region of strong coupling down-dip beneath Shikoku and Kyushu. Following this pattern, the new models produce less coseismic uplift offshore and greater subsidence inland, resulting in a tsunami that provides a more consistent match to historical observations and that is able to inundate Lake Ryuuoo with a great enough flow to produce the deposit we observe. These finding suggest that spatial trends in present-day

coupling models may be consistent with past periods of coseismic rupture along the Nankai Trough.

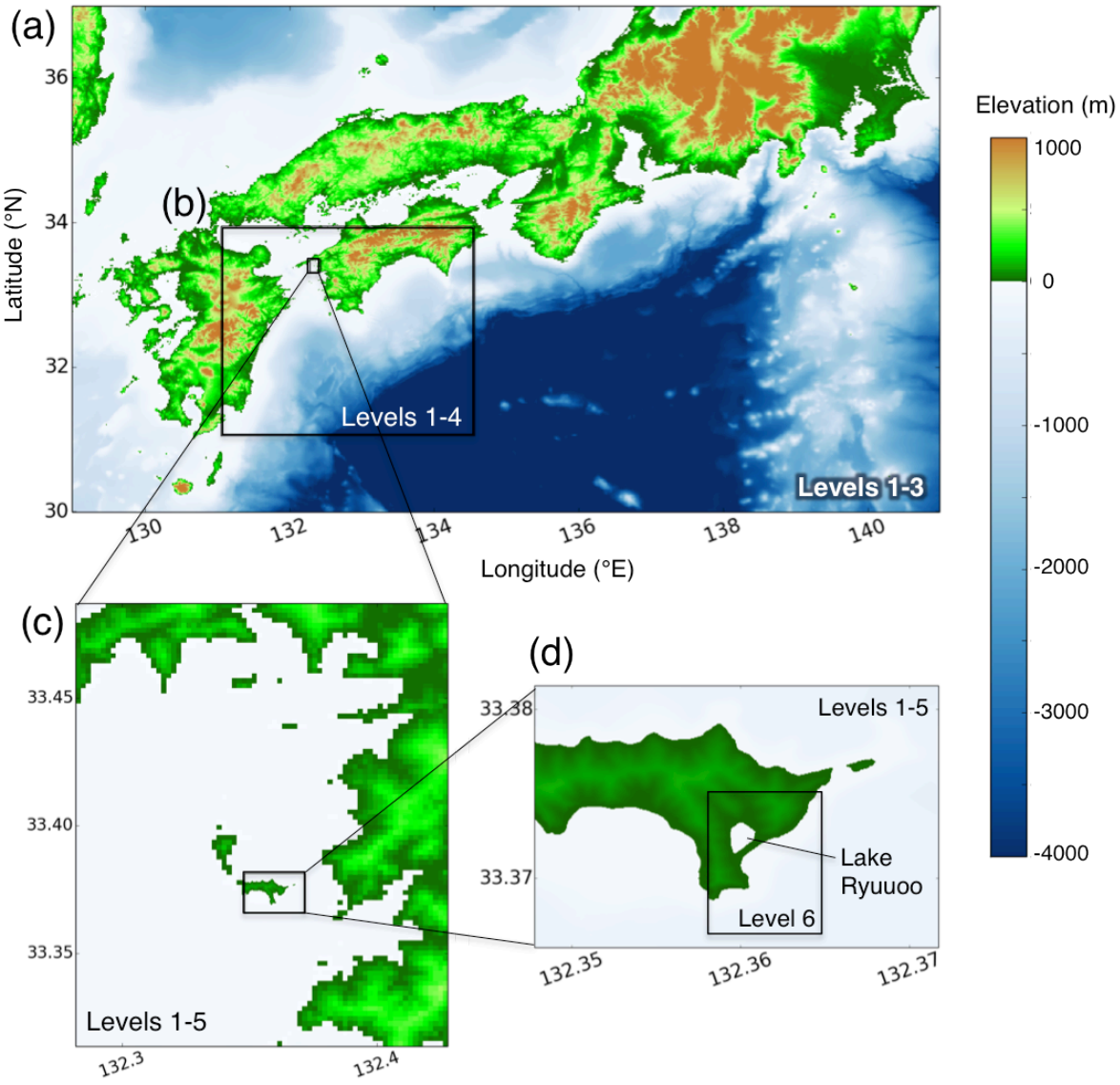

Figure 2.1. GeoClaw topography models and mesh configuration. Letters a – d show the four topography grids with differing resolutions described in the text. Level numbers indicate the level of adaptive mesh refinement allowed in each region, where the 6 levels of refinement have decreasing mesh sizes of ~50 km, ~25 km, ~4 km, ~500 m, ~250 m, and ~5 m.

Table 2.1. Fault parameters describing the Furumura et al. (2011) kinematic subfault model of C.E. 1707 Hōei earthquake.

Subfault segment	Top center location (°N, °E)	Depth (km)	Length (km)	Width (km)	Strike (°)	Dip (°)	Rake (°)	Slip (m)
N1	34.594, 138.559	6.4	120	50	193	20	71	5.6
N2	33.444, 137.226	4.1	215	100	246	10	113	7.0
N3	32.777, 135.290	7.8	155	100	251	12	113	5.6
N4’	32.400, 133.810	10.1	135	120	250	8	113	9.2
N5’	32.090, 132.780	10	70	80	250	8	118	9.2

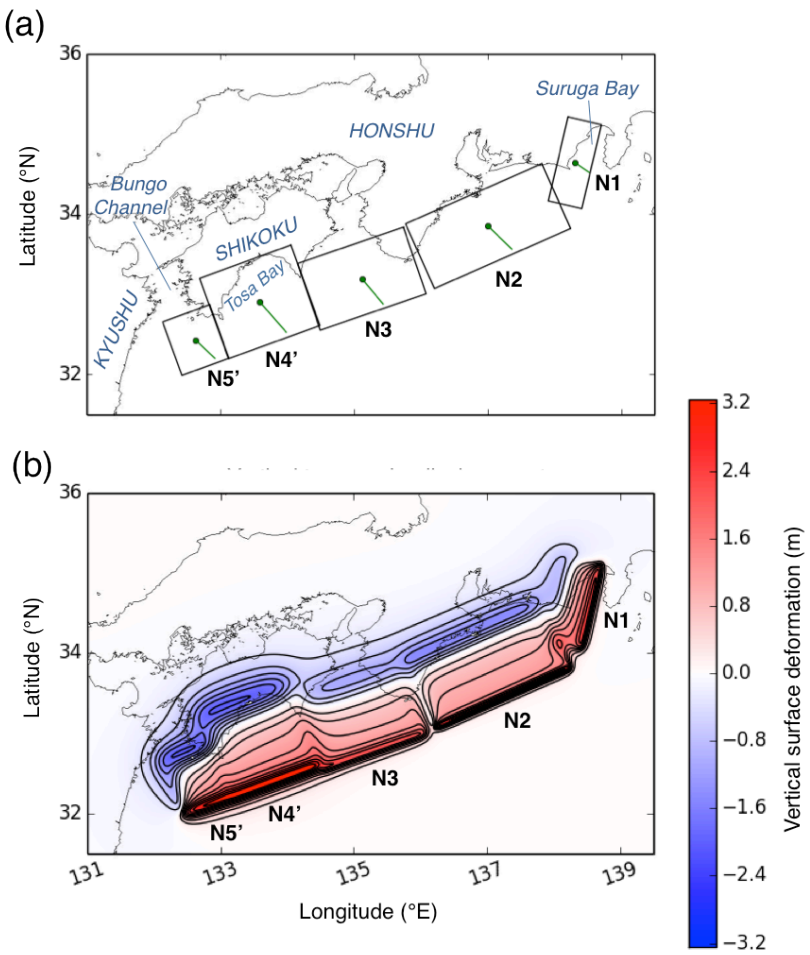

Figure 2.2. Furumura et al. (2011) earthquake source. (a) Black rectangles show the locations of the five subfault segments in the Furumura et al. (2011) Hōei earthquake model. Green lines indicate the rake of the slip vector on each plane's surface. (b) Okada solution for vertical topography displacement calculated from the Furumura et al. (2011) subfault model for the Hōei earthquake and used as the tsunami source in F11 GeoClaw simulations, where areas of subsidence are shown in blue, and areas of uplift are shown in red.

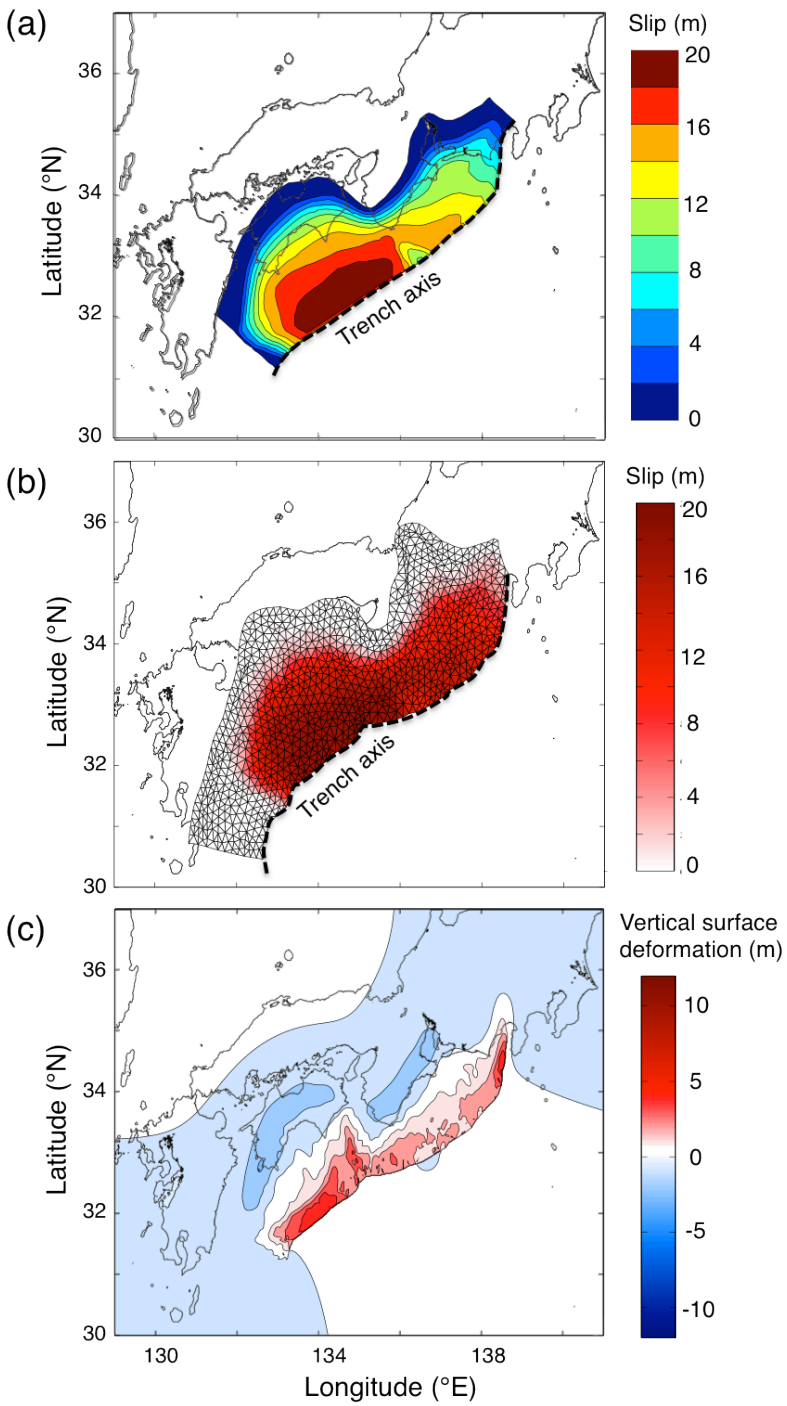

Figure 2.3. Hyodo and Hori (2013) earthquake source. (a) Coseismic slip distribution for the large earthquake scenario published in Hyodo and Hori (2013). (b) Slip magnitudes projected onto Nankai plate interface dislocation elements, triangulated from the geometry by Hirose et al. (2008). (c) Calculated vertical surface deformation used as the tsunami source in HH13 GeoClaw simulations, where areas of subsidence are shown in blue, and areas of uplift are shown in red.

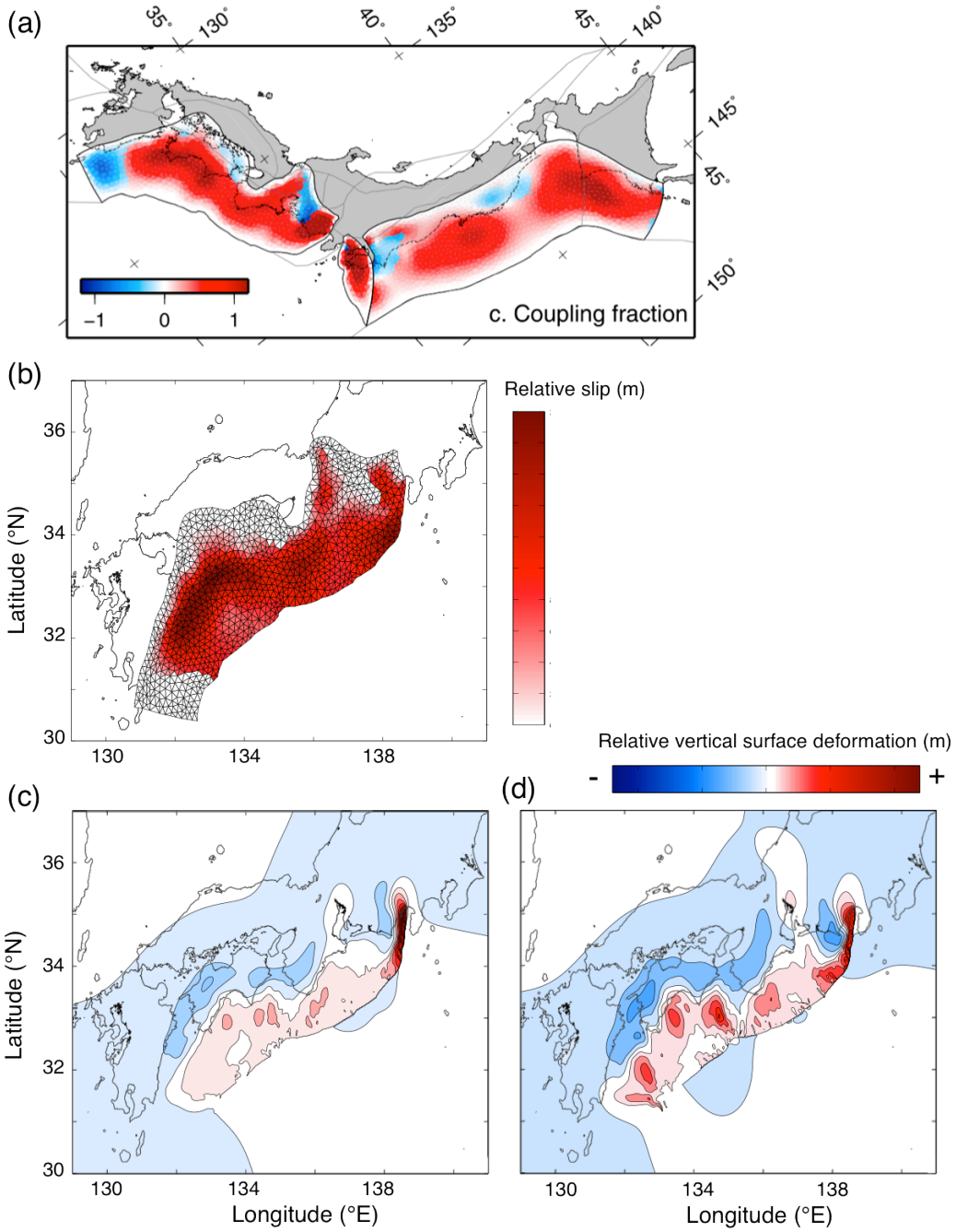

Figure 2.4. Coupling-based earthquake sources. (a) Interseismic coupling fractions from Loveless and Meade (2010) estimated on the Japan, Nankai, and Sagami subduction interfaces, where coupling fraction is defined as slip deficit divided by long-term plate motion (adapted from Fig. 10c in Loveless and Meade, 2010). (b) Coseismic slip distribution, scaled to match interseismic coupling fractions and projected onto Nankai plate interface dislocation elements triangulated from the geometry by Hirose et al. (2008). (c) Calculated vertical surface deformation, where the rake of slip was equal to the direction of long-term plate motion. (d) Calculated vertical surface deformation, where the rake of slip was equal to the direction of measured slip deficit.

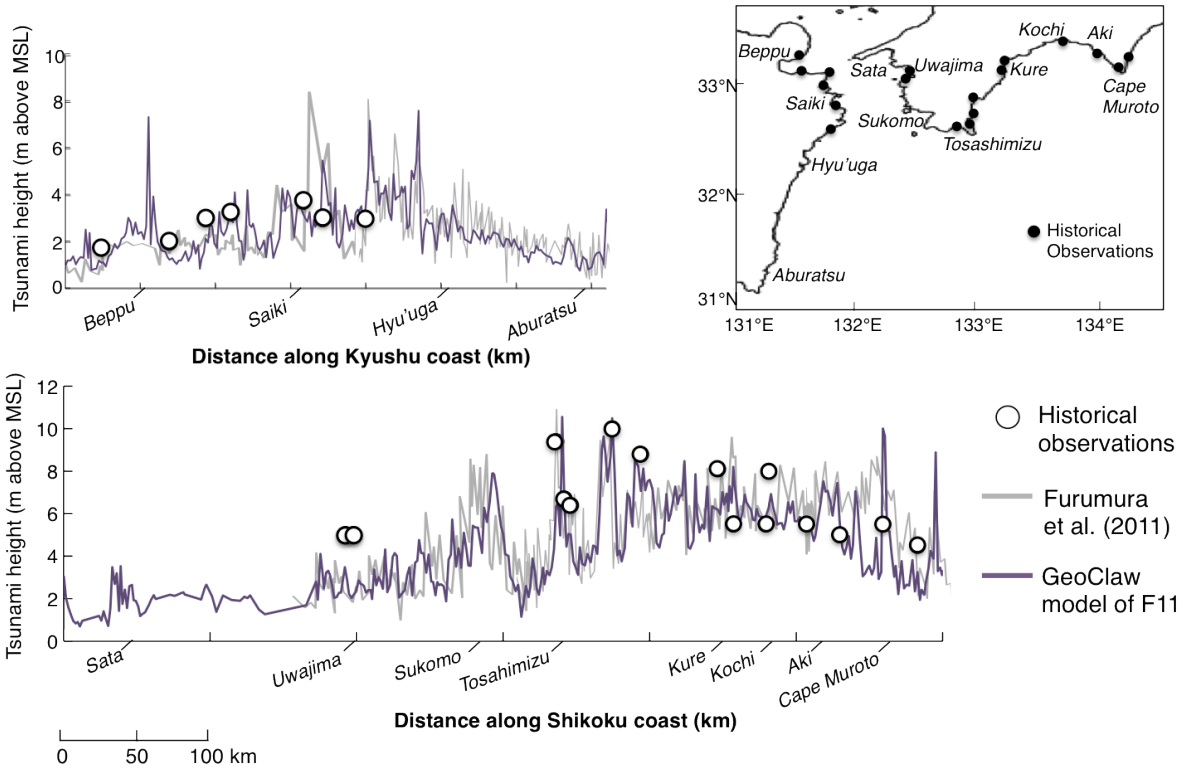

Figure 2.5. Maximum Hōei tsunami heights along the Pacific coast of southwestern Japan for the F11 earthquake scenario. Locations labeled on the horizontal axes are shown on the map in the upper-right. The purple line shows the GeoClaw calculation of maximum tsunami heights for the Furumura et al. (2011) subfault model. For validation, these results are compared to the tsunami heights originally presented in Furumura et al. (2011), calculated using a different tsunami model by Goto and Ogawa (1997). Open circles denote historical observations of C.E. 1707 tsunami height from Hatori (1988), and their locations are shown on the map in the upper-right.

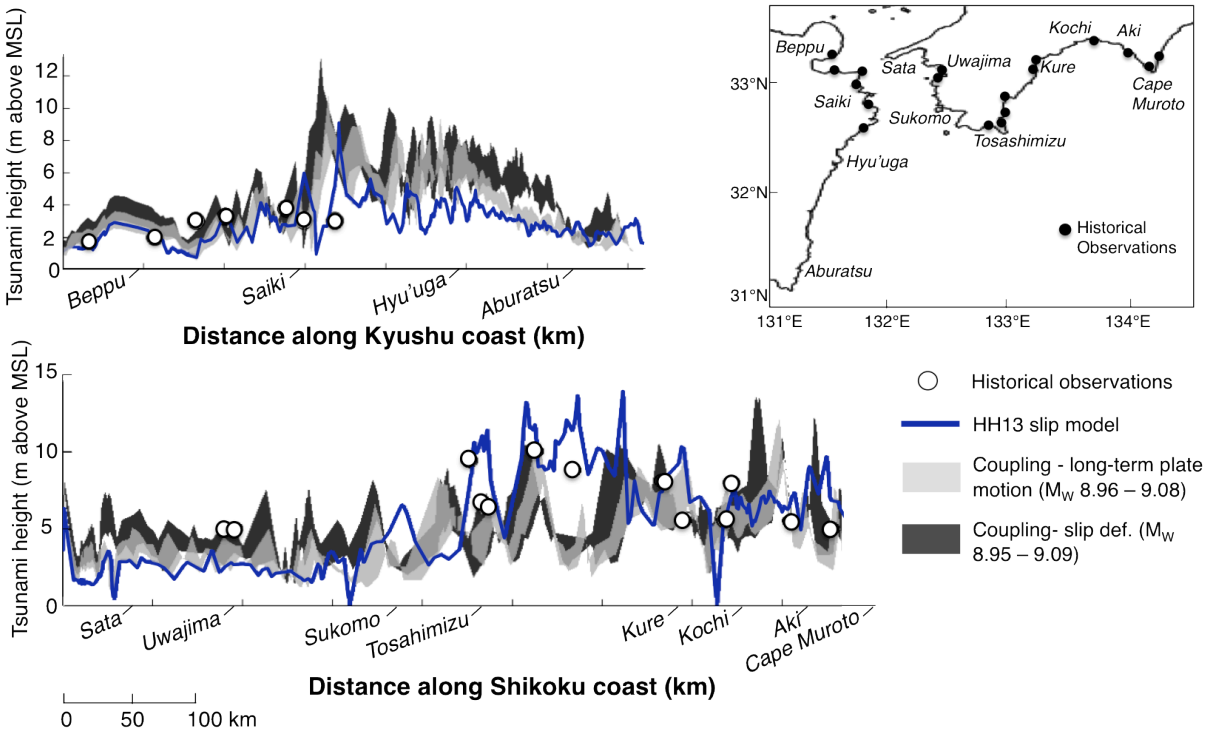

Figure 2.6. Maximum Hōei tsunami heights along the Pacific coast of southwestern Japan for the HH13 and coupling-based earthquake scenarios (following the same format as Fig. 2.5)**.**

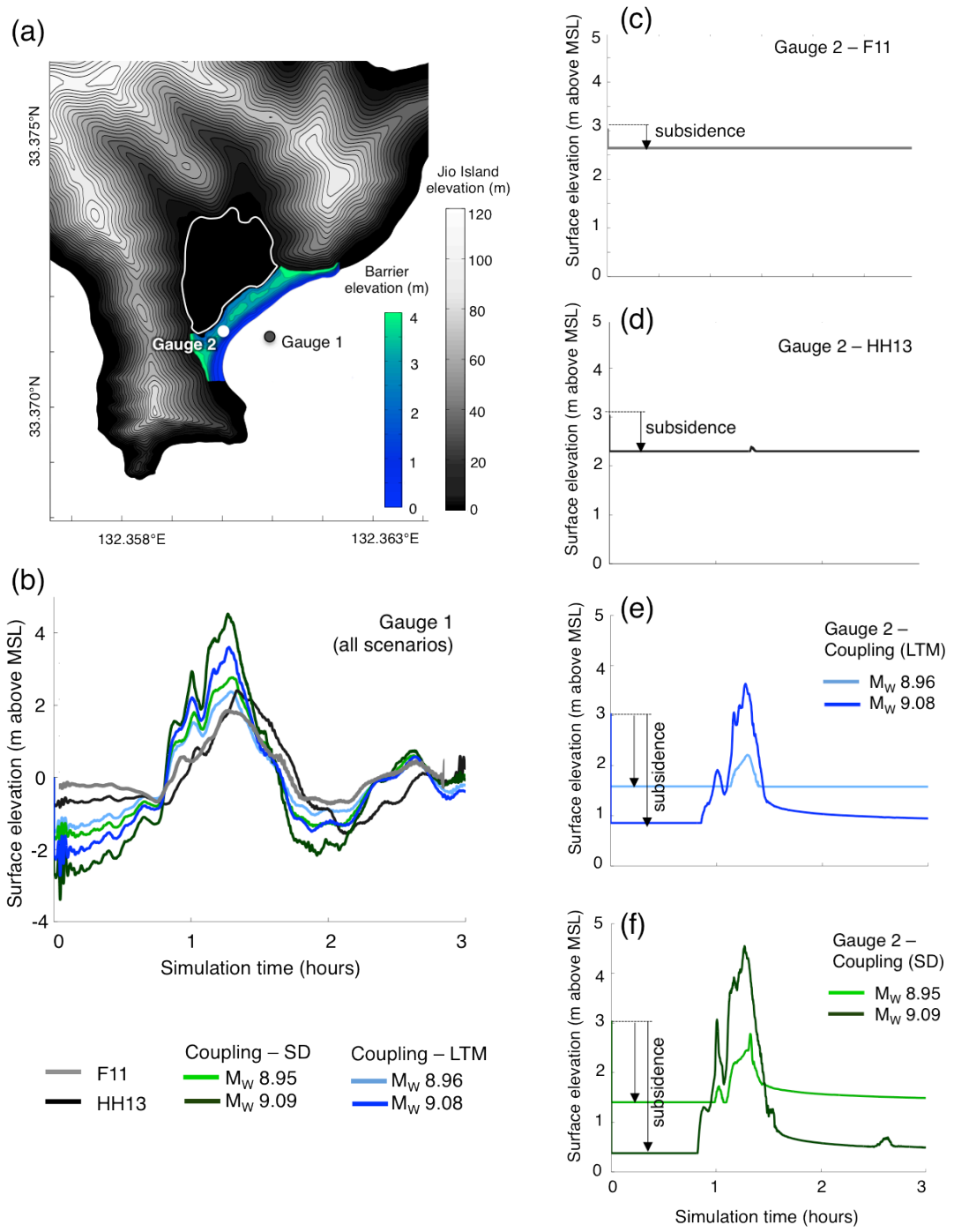

Figure 2.7. Model tide gauge results. (a) Contour map of Lake Ryuuoo showing locations of modeled gauges in GeoClaw tsunami simulations, where gauge 1 is located offshore and gauge 2 is on the lowest-elevation area of Lake Ryuuoo's barrier. (b) Gauge 1 results for the F11 scenario, the HH13 scenario, the two long-term plate motion coupling-based scenarios, and the two slip deficit coupling-based scenarios. (c) Gauge 2 results for all scenarios. Gauge 2 is initially located ~3 m above MSL (initial elevation indicated by black dashed lines), and coseismic subsidence causes the gauge's elevation to drop at the beginning of each simulation (subsidence indicated by black arrows).

REFERENCES

Amante, C., and B.W. Eakins (2009), ETOPO1 1 Arc-Minute Global Relief Model: Procedures, Data Sources and Analysis, *NOAA Technical Memorandum NESDIS SGDC-24.* National Geographic Data Center, NOAA, doi:10.7289/V5C8276M [accessed Feb. 17, 2015].

Ando, M. (1975), Source mechanisms and tectonic significance of historical earthquakes along the Nankai Trough, Japan, *Tectonophys., 27*, 119–140, doi:10.1016/0040-1951(75)90102-X.

An'naka, T., K. Inagaki, H. Tanaka, and K. Yanagisawa (2003), Characteristics of great earthquakes along the Nankai trough based on numerical tsunami simulation, *J. Earthq. Eng.* [CD-ROM]*, 27*, article 307 (in Japanese).

Arcos, M.E.M. and R.J. LeVeque (2015), Validating velocities in the GeoClaw tsunami model using observations hear Hawaii from the 2011 Tohoku tsunami, *Pure Appl. Geophys., 172,* 849-867, doi:10.1007/s00024-014-0980-y.

Atwater, B.F. (2005), *The Orphan Tsunami of 1700: Japanese Clues to a Parent Earthquake in North America,* U.S. Geological Survey.

Bahr, A., F. Larmy, H. Arz, H. Kuhlmann, and G. Wefer (2005), Late glacial to Holocene climate and sedimentation history in the NW Black Sea, *Mar. Geol., 214(4)*, 309-322, doi:10.1016/j.margeo.2004/11.013.

Berger, M.J., D.L. George, R.J. LeVeque, and K.T. Mandli (2011), The GeoClaw software for depth-averaged flows with adaptive refinement, *Adv. Water Res., 34,* 1195-1206, doi:10.1016/j.advwatres.2011.02.016.

Boldt, K.V., P. Lane, J.D. Woodruff, and J.P. Donnelly (2010), Calibrating a sedimentary record of overwash from southeastern New England using modeled historic hurricane surges, *Mar. Geol., 275(1-4),* 127-139, doi:10.1016/j.margeo.2010.05.002.

Bowen, H.J.M. (1956), Strontium and barium in seawater and marine organisms, *J. of the Mar. Biol. Assoc. of the United Kingdom, 35,* 451-460.

Brandon, C. M., J.D. Woodruff, D. Land, and J.P. Donnelly (2013), Tropical cyclone and wind speed constraints from resultant storm surge deposition: A 2500 year reconstruction of hurricane activity from St. Marks, FL, *Geochm, Geophys. Geosyst., 14*, 2993-3008.

Brandon, C., J.D. Woodruff, and J.P. Donnelly (2014), How unique was Hurricane Sandy? Sedimentary reconstructions of extreme flooding from New York Harbor, *Sci. Rep., 4: 7366*, doi: 10.1038/srep07366.

Bürgmann, R., M.G. Kogan, G.M. Steblov, G. Hilley, V.E. Levin, and E. Apel (2005), Interseismic coupling and asperity distribution along the Kamchatka subduction zone, *J. Geophys.Res., 110,* B07405, doi:10.1029/2005JB003648.

Buynevich, I.V. (2011), Heavy minerals add weight to neoichnological research, *Palaios, 26,* 189-191, doi:10.2110/palo.2011.S01.

Cabinet Office (2012), Anticipated damages due to the Nankai Trough mega-thrust earthquake (second report), http://bousai.go.jp/jishin/nankai/taisaku/pdf/1_1.pdf, accessed Aug. 1, 2015.

Chagué-Goff, C., S. Dawson, J.R. Goff, J. Zachariasen, K.R. Berryman, D.L. Garnett, H.M. Waldron, and D.C. Mildenhall (2002), A tsunami (C. 6300 years BP) and other environmental changes, northern Hawke's Bay, New Zealand, *Sediment. Geol., 150(1),* 89-102, doi: 10.1016/S0037-0738(01)00269-X.

Chagué-Goff, C., A. Andrew, W. Szczuciński, J. Goff, and Y. Nishimura (2012), Geochemical signatures up to the maximum inundation of the 2011 Tohoku-oki tsunami – Implications for the 869 AD Jogan and other paleotsunamis, *Sediment. Geol., 282,* 65-77, doi:10.1016/j.sedgeo.2012.05.021.

Cheng, W., and R. Weiss (2013), On sediment extent and runup of tsunami waves, *Earth and Planet. Sci. Let., 362,* 306-309, doi:10.1016/j.epsl.2012.12.004.

Chu, J.H., C.R. Sampson, A.S. Levine, and E. Fukada (2002), The joint typhoon warning center tropical cyclone best-tracks, 1945–2000, Ref. NRL/MR/7540-02-16, Nav. Res. Lab., Washington, D.C.

Colinvaux, P., P.E. De Oliveira, and P. Moreno (1999), *Amazon Pollen Manual and Atlas*, Hardwood Academic Publishers, Amsterdam, Netherlands (NLD).

Croudace, I.W., A. Rindby, and R.G. Rothwell (2006), ITRAX: description and evaluation of a new multi-function X-ray core scanner, *Geol. Soc. Lond. Spec. Publ., 267*, 51-63, doi:10.1144/GSL.SP.2006.2.67.01.04.

Dean, W. E. (1974), Determination of carbonate and organic matter in calcareous sediments and sedimentary rocks by loss on ignition: comparison with other methods, *J. of Sediment. Petrol., 44*, 242-248.

Donnelly, J.P., J. Butler, S. Roll, M. Wengren, and T. Webb (2004), A backbarrier overwash record of intense storms from Brigantine, New Jersey, *Mar. Geol., 210*, 107-121, doi:10.1016/j.margeo.2004.05.005.

Donnelly, J.P., N. Kraus, and M. Larson (2006), State of knowledge on measurement and modeling of coastal overwash, *J. of Coast. Res., 22,* 965-991, doi:10.211/04-0431.1.

Donnelly, J.P., and J.D. Woodruff (2007), Intense hurricane activity over the past 5,000 years controlled by El Niño and the West African monsoon, *Nature*, *447,* 465-468.

El-Fiky, G., and T. Kato (2006), Secular crustal deformation and interplate coupling of the Japanese Islands as deduced from continuous GPS array, 1996-2001, *Tectonophys., 422,* 1-22.

Ferguson, R.I., and M. Church (2004), A simple universal equation for grain settling velocity, *J. of Sediment. Res., 74.6,* 933-937.

Fitch, T.J. (1972), Plate convergence, transcurrent faults, and internal deformation adjacent to southeast Asia and the western Pacific, *J. Geophys. Res., 77(23),* 4432-4460, doi:10.1029/JB077i023p04432.

Fritz, H.M., J.C. Borrero, C.E. Synolakis, E.A. Okal, R. Weiss, V.V. Titov, B.E. Jaffe, S. Foteinis, P.J. Lynett, I. Chan, and P.L. Liu (2011), Insights on the 2009 South Pacific tsunami in Samoa and Tonga from field surveys and numerical simulations, *Earth Sci. Rev., 107*, 66-75, doi:10.1016/j.earscirev.2011.03.004.

Fujiwara, T., S. Kodaira, T. No, Y. Kaiho, N. Takahashi, and Y. Kaneda (2011), The 2011 Tohoku-oki earthquake: displacement reaching the trench axis. *Science, 334*, 1240, doi:10.1126/science.1211554.

Furumura, T., K. Imai, and T. Maeda (2011), A revised tsunami source model for the 1707 Hoei earthquake and simulation of tsunami inundation of Ryujin Lake, Kyushu, Japan, *J. Geophys. Res.*, *116*, B02308, doi: 10.1029/2010JB007918.

Goff, J., C. Chagué-Goff, S. Nichol, B. Jaffe, and D. Dominey-Howes (2012), Progress in paloetsunami research, *Sediment. Geol., 243-244,* 70-88, doi:10.1016/j.sedgeo.2011.11.002.

GeoClaw Authors (2015), GeoClaw software, version 5.3.0, http://clawpack.org/geoclaw.

George, D.L. (2006), Finite volume methods and adaptive refinement for tsunami propagation and inundation. PhD thesis, University of Washington.

George, D.L. and R.J. LeVeque (2006), Finite volume methods and adaptive refinement for global tsunami propagation and local inundation, *Sci. of Tsunami Hazards, 24*, 319-328.

George, D.L. (2008), Augmented Riemann solvers for the shallow water equations over variable topography with steady states and inundation, *J. Comput. Phys., 227,* 3089-3113, doi:10.1016/j.jcp.2007.10.027.

González, G., R.J. LeVeque, J. Varkovitzky, P. Chamberlain, B. Hirai, and D.L. George (2011), GeoClaw Results for the NTHMP Tsunami Benchmark Problems. http://www.clawpack.org/links/nthmp-benchmarks/geoclaw-results.

Goto, C., and Y. Ogawa (1997), *IUGG/IOC TIME PROJECT: Numerical Method of Tsunami Simulation with the Leap-Frog Scheme – Part I: Shallow Water Theory and Its Difference Scheme, Manuals and Guides,* vol. 35, 43 pp., U. N. Educ., Sci. and Cult. Organ., Paris.

Goto, K., C. Chague-Goff, S. Fujino, J. Goff, B. Jaffe, Y. Nishimura, B. Richmond, D. Sugawara, W. Szczucinski, D. Tappin, R. Witter, and E. Yulianto (2011), New insights of tsunami hazard from the 2011 Tohoku-oki event, *Mar. Geol.*, *290*, 46-40, doi: 10.1016/j.margeo.2011.10.004.

Goto, K., C. Chague-Goff, G. Goff, and B. Jaffe (2012), The future of tsunami research following the 2011 Tohoku-oki event, *Sediment. Geol.*, *282*, 1-13, doi:10.1016/j.sedgeo.2012.08.003.

Hashimoto, C., T. Sagiya, and M. Matsuura (2009), Interplate coupling in southwest Japan inferred from GPS data inversion, paper presented at Fall Meeting, Seismol. Soc. of Jpn., Kyoto, Japan.

Haslett, J., and A. Parnell (2008), A simple monotone process with application to radiocarbon-dated depth chronologies, *J. of the Royal Stat. Soc.: Series C (Applied Statistics), 57(4)*, 399-418, doi:10.1111/j.1467-9876.2008.00623.x.

Hatori, T. (1985), Field investigation of the 1596 Bungo tsunami along the coast of Beppu Bay, Kyushu, *Bull. of Earthq. Res. Inst., Univ. of Tokyo*, *60,* 429-438 (in Japanese).

Hatori, T. (1988), Tsunami behaviors in the Seto Inland Sea and Bungo Channel caused by the Nankaido earthquakes in 1707, 1854, and 1946.

Heki, K., and S. Miyazaki (2001), Plate convergence and long-term crustal deformation in central Japan, *Geophys. Res. Lett., 28(12),* 2313-2316, doi:10.1029/2000GL012537.

Hirose, F., J. Nakajima, and A. Hasegawa (2008), Three-dimensional seismic velocity structure and configuration of the Philippine Sea slab in southwestern Japan estimated by double-difference tomography, *J. Geophys. Res., 113,* B09315, doi:10.1029/2007JB005274.

Hok, S., E. Fukuyama, and C. Hashimoto (2011), Dynamic rupture scenarios of anticipated Nankai-Tonankai earthquakes, southwest Japan, *J. of Geophys. Res., 116,* B12319, doi:10.1029/2011JB008492.

Holland, T.K., R.A. Holman, and A.H. Sallenger Jr. (1991), Estimation of overwash bore velocities using video techniques, *in* Kraus, N.C., K.J. Gingerich, and D.L. Kriebel, eds., Coastal Sediments (1991): Seattle, Washington, American Society of Civil Engineers, 489-497.

Hyodo, M. and T. Hori (2013), Re-examination of possible great interpolate earthquake scenarios in the Nankai Trough, southwest Japan, based on recent findings and numerical simulations, *Tectonophys., 600,* 175-186, doi:10.1016/j.tecto.2013.02.038.

Hyodo, M., T. Hori, K. Ando, and T. Baba (2014), The possibility of deeper or shallower extent of the source area of Nankai Trough earthquakes based on the 1707 Hoei tsunami heights along the Pacific and Seto Inland Sea coasts, southwest Japan, *Earth, Planets, and Space, 66(123),* doi:10.1186/1880-5981-66-123.

Ishibashi, K. (2002), Great Tokai and Nankai, Japan, earthquakes as boundary conditions for the Philippine Sea slab: Review from historical seismology, in *Proc. Meeting 13K-7* (DPRI, Kyoto Univ.), 1-9 (in Japanese with English abstract).

Ishibashi, K. (2004), Status of historical seismology in Japan, *Ann. of Geophys.*, *47,* 339–368.

Ishibe, T. and K. Shimazaki (2005), Estimation of the Source of Tsunami Accompanied by the 1596 Keicho-Bungo Earthquake, *Hist. Earthq.*, *20*, 119-131 (in Japanese with English abstract).

Ito, T., and M. Hashimoto (2004), Spatiotemporal distribution of interplate coupling in southwest Japan from inversion of geodetic data, *J. Geophys. Res., 109,* B02315, doi:10.1029/2002JB002358.

Jaffe, B.E. and G. Gelfenbaum (2007), A simple model for calculating tsunami flow speed from tsunami deposits, *Sediment. Geol., 200,* 347-361, doi:10.1016/j.sedgeo.2007.01.013.

Jaffe, B.E., K. Goto, D. Sugawara, B.M. Richmond, S. Fujino, and Y. Nishimura (2012), Flow speed estimated by inverse modeling of sandy tsunami deposits: results from the 11 March 2011 tsunami on the coastal plain near the Sendai Airport, Honshu, Japan, *Sediment. Geol., 282,* 90-109, doi:10.1016/j.sed.geo.2012.09.002.

Japan Coast Guard. *Yawatahama Ko and Approaches* [map]. 1:30,000. Tokyo, Japan: Japan Coast Guard, 2001.

Kanai, Y. and Y. Inouchi (2004), Sedimentation rates and environmental changes of Lakes Amida and Kamegaike, Ehime Prefecture, Japan, *J. of the Sediment. Soc. of Jpn., 58,* 93-103.

Kaneko, Y., J.-P. Avouac, and N. Lapusta (2010), Towards inferring earthquake patterns from geodetic observations of interseismic coupling, *Nature Geosci., 3,* 363-369, doi:10.1038/ngeo843.

Kirwan, M.L., A.B. Murray, J.P. Donnelly, and D.R. Corbett (2011), Rapid wetland expansion during European settlement and its implication for marsh survival under modern sediment delivery rates, *Geol., 39(5),* 507-510.

Le Pichon, X., S. Mazzotti, P. Henry, and M. Hashimoto (1998), Deformation of the Japanese Islands and seismic coupling: An interpretation based on GSI permanent GPS observations, *Geophys. J. Int., 134(2),* 501-514, doi:10.1046/j.1365-246x.1998.00595.x.

LeVeque, R.J. and D.L. George (2007), High-resolution finite volume methods for the shallow water equatiosn with bathymetry and dry states. In: Liu, P.L.F., H. Yeh, and C. Synolakis (eds.). Advanced Numerical Models for Simulating Tsunami Waves and Runup, *vol. 10*, 43-73.

LeVeque, R.J., D.L. George, and M.J. Berger (2011), Tsunami modeling with adaptively refined finite volume methods, *Acta Numerica,* 211-289, doi:10.1017/S0962492911000043.

Liu, K. and M.L. Fearn (1993), Lake-sediment record of late Holocene hurricane activities from coastal Alabama, *Geol., 21(9)*, 793-796.

Liu, Z., S. Owen, D. Dong, P. Lundgren, F. Webb, E. Hetland, and M. Simons (2010), Integration of transient strain events with models of plate coupling and areas of great earthquakes in southwestern Japan, *Geophys. J. Int., 181,* 1292-1312, doi:10.1111/j.1365-246X.2010.04599.x.

Loveless, J.P. and B.J. Meade (2010), Geodetic imaging of plate motions, slip rates, and partitioning of deformation in Japan, *J. of Geophys. Res., 115*, B02410, doi:10.1029/2008JB006248.

Loveless, J.P. and B.J. Meade (2011), Spatial correlation of interseismic coupling and coseismic rupture extent of the 2011 M_W = 9.0 Tohoku-oki earthquake, *Geophys. Res. Lett., 38,* L17306, doi:10.1029/2011GL048561.

Mayer, L.M., L.L. Schick, A.A. Mead, K.C. Ruttenberg, and S.J. Bentley (2007), Marine vs. terrigenous organic matter in Louisiana coastal sediments: The uses of bromine: organic carbon ratios, *Mar. Chem., 107(2)*, 244-254.

Mayer, L.M., S.A. Macko, W.H. Mook, and S. Murray (1981), The distribution of bromine in coastal sediments and its use as a source indicator for organic matter, *Org. Geochem.*, *3(1),* 37-42.

Mazzotti, S., X. Le Pichon, P. Henry, and S. Miyazaki (2000), Full interseismic locking of the Nankai and Japan-west Kurile subduction zones: An analysis of uniform elastic strain accumulation in Japan constrained by permanent GPS, *J. Geophys. Res., 105(B6)*, 13,159-13,177, doi:10.1029/2000JB900060.

Meade, B., and J.P. Loveless (2009), Block modeling with multiple fault network geometries and a linear elastic coupling estimator in spherical coordinates, *Bull. Seismol. Soc. Amer., 99(6),* 3124-3139.

Minoura, K., F. Imamura, T. Takahashi, N. Shuto (1997), Sequence of sedimentation processes caused by the 1992 Flores tsunami: evidence from Babi Island, *Geol., 25,* 523-526, doi: 10.1130/0091-7613(1997)025<0523:SOSPCB>2.3.CO;2.

Miyamoto, D., H. Murakami, Y. Kozuki, and T. Kubo (2006), The effect of earth tide, incident angle and periods of tsunamis on the behavior of tsunamis in the Seto Inland Sea (in Japanese), *Proc. Coastal Eng., JSCE 53*, 261-265.

Miyazaki, S., and K. Heki (2001), Crustal velocity field of southwest Japan: Subduction and arc-arc collision, *J. Geophys. Res., 106(B3),* 4305-4326, doi:10.1029/2000JB900312.

Murakami, H., S. Itoh, Y. Hiraiwa, and T. Shimada (1995), Re-examination of historical tsunamis in Shikoku Island, Japan, in *Tsunami: Progress in Prediction, Disaster Prevention and Warning*, edited by Y. Tsuchiya and N. Shuto, 197-210, Kluwer Academic Publishers, Netherlands.

Nakada, M., N. Yonekura, and K. Lambeck (1991), Late Pleistocene and Holocene sea-level changes in Japan: implications for tectonic histories and mantle rheology, *Palaeogeogr., Palaeoclimatology, Palaeoecol., 85*, 107-122, doi:10.1016/0031-0182(91)90028-P.

Nanayama, F., A. Kaga, H. Kinoshita, Y. Yokoyama, K. Satake, T. Nakata, Y. Sugiyama, and E. Tsukuda (2002), Tsunami traces discovered in Tomogashima Island, Kitan Strait, central Japan, *Kaiyo Month. Symp*., 123–131 (in Japanese).

Okada, A. (1973), On the Quaternary faulting along the Median Tectonic Line fault system in the northwestern part of Shikoku, *Bull. Fac. Liter. Aichi Prefect. Univ., 23*, 68-94, (in Japanese).

Okada, A. (1980), Quaternary faulting along the Median Tectonic Line of southwest Japan, in *Median Tectonic Line of southwest Japan*, edited by K. Ichikawa, memoir 18, 79-108, Mem. Geol. Soc. Jpn.

Okada, Y. (1985), Surface deformation due to shear and tensile faults in a half-space, *Bull. of the Seismol. Soc. of America, 75(4)*, 1135-1154.

Okamura, M., H. Matsuoka, N. Chida, and K. Shimazaki (2004), Recurrence intervals of super Nankai earthquakes, paper presented at Fall Meeting, *Seismol. Soc. Jpn*., Fukuoka, Japan.

Oshima District town hall (2008), *Oshima Rekishi Nenpyo [Chronicles of Oshima],* (informal town document, read on site, July 23, 2014).

Parnell, A.C., J. Haslett, J.R.M. Allen, C.E. Buck, and B. Huntley (2008), A flexible approach to assessing synchroneity of past events using Bayesian reconstructions of sedimentation history, *Quat. Sci. Rev., 27*, 1872-1885, doi:10.1016/j.quascirev.2008.07.009.

Pennington, W., T.G. Tutin, R.S. Cambray, and E.M. Fisher (1973), Observations on lake sediments using fallout ^{137}Cs as a tracer, *Nature*, *242*, 324-326, doi:10.1038/242324a0.

Peters, R., B. Jaffe, and G. Gelfenbaum (2007), Distribution and sedimentary characteristics of tsunami deposits along the Cascadia margin of western North America, *Sediment. Geol., 200*, 372-386, doi:10.1016/j.sedgeo.2007.01.015.

Peterson, L.C., G.H. Haug, K.A. Hughen, and U. Rohl (2000), Rapid changes in the hydrological cycle of the tropical Atlantic during the last glacial, *Science, 290*, 1947-1950.

Reimer, P.J., E. Bard, A. Bayliss, J.W. Beck, P.G. Blackwell, C.B. Ramsey, C.E. Buck, H. Cheng, R.L. Edwards, and M. Friedrich (2013), IntCal13 and Marine13 radiocarbon age calibration curves 0–50,000 years cal BP, *Radiocarbon*, *55(4),* 869-1887, doi:10.2458/azu_js_rc.55.16947.

Research Group for Active Faults in Japan (1991), *Active Faults in Japan: Sheet Maps and Inventories*, rev. ed., Univ. of Tokyo Press, Tokyo, (in Japanese).

Sakaguchi, A., F. Chester, D. Curewitz, O. Fabbri, D. Goldsby, G. Kimura, C.F. Li, Y. Masaki, E.J. Screaton, A. Tsutsumi, K. Ujiie, and A. Yamaguchi (2011), Seismic slip propagation to the up-dip end of plate boundary subduction interface faults: vitrinite reflectance geothermometry on Integrated Ocean Drilling Program NanTroSEIZE cores, *Geol., 39,* 395-398, doi:10.1130/G31642.1.

Savage, J.C., and W. Thatcher (1992), Interseismic deformation at the Nankai trough, Japan, subduction zone*, J. Geophys. Res., 97(B7),* 11,117–11,135, doi:10.1029/92JB00810.

Scileppi, E., and J.P. Donnelly (2007), Sedimentary evidence of hurricane strikes in western Long Island, New York, *Geochem., Geophys., Geosyst., 8,* QO6011, doi:10.1029/2006GC001463.

Shanahan, T.M., J.T. Overpeck, J.B. Hubeny, J. King, F.S. Hu, K. Hughen, G. Miller, and J. Black (2008), Scanning micro-X-ray fluorescence elemental mapping: A new tool for the study of laminated sediment records, *Geochem., Geophys., Geosyst., 9(2)*.

Sugawara, D., K. Goto, F. Imamura, H. Matsumoto, and K. Minoura (2011), Assessing the magnitude of the 869 Jogan tsunami using sedimentary deposits: Prediction and consequences of the 2011 Tohoku-oki tsunami, *Sediment. Geol.*, *282*, 14-26, doi:10.1016/j.sedgeo.2012.08.001.

Tabei, T., M. Adachi, S. Miyazaki, T. Watanabe, and S. Kato (2007), Interseismic deformation of the Nankai subduction zone, southwest Japan, inferred from three-dimensional crustal velocity fields, *Earth Planets Space, 59,* 1073-1082.

Tang, L., V.V. Titov, and C.D. Chamberlin (2009), Development testing, and applications of site-specific tsunami inundation models for real-time forcasting, *J. of Geophys. Res., 114,* doi:10.1029/2009JC005476.

Tsutsumi, H., and A. Okada (1996), Segmentation and Holocene surface faulting on the Median Tectonic Line, southwest Japan, *J. of Geophys. Res.: Solid Earth (1978-2012),* 101(B3), 5855-5871, doi:10.1029/95JB01913.

Usami, T. (1987), *Descriptive catalogue of disaster earthquakes in Japan*, Univ. of Tokyo Press, Tokyo.

USGS (2006), Shuttle Radar Topography Mission, 3 Arc Second scene N33E132, Global Land Cover Facility, Univ. of Maryland, College Park, Maryland, February 2000.

Vlag, P.A., P.P. Kruiver, M.J. Dekkers (2004), Evaluating climate change by multivariate statistical techniques on magnetic and chemical properties of marine sediments (Azores region), *Palaeogeog., Palaeoclimatology, Palaeoecol., 212*, 23-44, doi:10.1016/j.paeaeo.2004.05.015.

Wallace, D.J., J.D. Woodruff, J.B. Anderson, and J.P. Donnelly (2014), Palaeohurricane reconstructions from sedimentary archives along the Gulf of Mexico, Caribbean Sea, and western North Atlantic Ocean margins, in *Sedimentary Coastal Zones from High to Low Latitudes: Similarities and Differences,* edited by I.P. Martini and H.R. Wanless, 481-501, Geological Society, London, Special Publications 388.

Woodruff, J.D., J.P. Donnelly, S. Mohrig, and W.R. Geyer (2008), Reconstructing relative flooding intensities responsible for hurricane-induced deposits from Laguna Playa Grande, Vieques, Puerto Rico, *Geol., 36(5)*, 391-394, doi:10.1130/G24731A.1.

Woodruff, J.D., J.P. Donnelly, and A. Okusu (2009), Exploring typhoon variability over the mid-to-late Holocene: evidence of extreme coastal flooding from Kamikoshiki, Japan, *Quat. Sci. Rev., 28*, 1774-1785, doi:10.1016/j.quascirev.2009.02.005.

Woodruff, J.D., J. Irish, and S. Camargo (2013), Coastal flooding by tropical cyclones and sea-level rise, *Nature*, *504*, 44-52, doi:10.1038/nature12855.

Woodruff, J.D., K. Kanamaru, S. Kundu, and T. Cook (2015), Depositional evidence for the Kamikaze typhoons and links to changes in typhoon climatology, *Geol.*, *43(1),* 91-94, doi:10.1130/G36209.1.

Wright, C., and A. Mella (1963), Modifications to the Soil Pattern of South-Central Chile Resulting from Seismic and Associated Phenomena during the Period May to August, 1960, *Bull. Seismolog. Soc. Am., 53,* 1367-1402.

Ziegler, M., T. Jilbert, G.J. de Lange, L.J. Lourens, and G.J. Reichart (2008), Bromine counts from XRF scanning as an estimate of the marine organic carbon content of sediment cores, *Geochem., Geophys., Geosyst., 9(5),* doi:10.1029/2007GC001932.